



HAL
open science

History of subduction polarity reversal during arc-continent collision: 1 constraints from the Andaman Ophiolite and its metamorphic sole

Alexis Plunder, Debaditya Bandyopadhyay, Morgan M Ganerød, Eldert L Advokaat, Biswajit Ghosh, Pinaki Bandopadhyay, Douwe van Hinsbergen

► To cite this version:

Alexis Plunder, Debaditya Bandyopadhyay, Morgan M Ganerød, Eldert L Advokaat, Biswajit Ghosh, et al.. History of subduction polarity reversal during arc-continent collision: 1 constraints from the Andaman Ophiolite and its metamorphic sole. *Tectonics*, 2020. hal-02524092

HAL Id: hal-02524092

<https://brgm.hal.science/hal-02524092>

Submitted on 30 Mar 2020

HAL is a multi-disciplinary open access archive for the deposit and dissemination of scientific research documents, whether they are published or not. The documents may come from teaching and research institutions in France or abroad, or from public or private research centers.

L'archive ouverte pluridisciplinaire **HAL**, est destinée au dépôt et à la diffusion de documents scientifiques de niveau recherche, publiés ou non, émanant des établissements d'enseignement et de recherche français ou étrangers, des laboratoires publics ou privés.

1 ***History of subduction polarity reversal during arc-continent collision:***
2 ***constraints from the Andaman Ophiolite and its metamorphic sole***

3
4 Alexis Plunder^{1,2}, Debaditya Bandyopadhyay^{3,4}, Morgan Ganerød⁵, Eldert L. Advokaat^{1,6},
5 Biswajit Ghosh³, Pinaki Bandopadhyay³ and Douwe J.J. van Hinsbergen¹

6
7 ¹Department of Earth Sciences, Utrecht University, Princetonlaan 8A, 3584 CB Utrecht, the Netherlands

8 ²BRGM, F-45060, Orléans, France

9 ³Department of Geology, University of Calcutta, 35 Ballygunge Circular Road, Kolkata, 700019, India

10 ⁴Department of Geology, University of North Bengal, Darjeeling-734013, India

11 ⁵Geological Survey of Norway NGU, Leiv Eirikssons Vei 39, 7491 Trondheim, Norway

12 ⁶Department of Physical Geography, Utrecht University, Princetonlaan 8A, 3584 CB Utrecht, the Netherlands

13

14 Corresponding author: Alexis Plunder (a.plunder@brgm.fr)

15

16 **Key Points:**

- 17 • We document the condition of formation of the metamorphic sole of the Andaman Island
18 Ophiolite
19 • We provide Ar/Ar ages for the subduction initiation leading to the formation of the
20 Andaman Island Ophiolite
21 • We estimate the duration of subduction polarity reversal following an arc continent
22 collision to 6 million years at least

23

24 **Abstract**

25 *Subduction polarity reversal during arc-continent collision has been proposed as a key*
26 *mechanism to initiate new subduction zones. Despite often interpreted, well-exposed geological*
27 *record that document the reversal are sparse. The ophiolitic lithounits of the Andaman and*
28 *Nicobar Islands have been proposed to have formed during the initiation of a new subduction*
29 *zone following the collision of the Woyla arc of Sumatra with Sundaland (Eurasia). We here*
30 *present new field, petrological and geochronological data to evaluate the timing of the initiation*
31 *of Andaman subduction. We targeted the previously inferred but unstudied metamorphic sole of*
32 *the Andaman Ophiolites that witnessed juvenile subduction. Thermodynamic modelling reveals*
33 *that the exposed amphibolites of the sole formed at around 0.9 GPa and 675°C. We dated two*
34 *samples of the metamorphic sole using the Ar/Ar method on amphibole, giving cooling ages of*
35 *106.4 ± 2.1 Ma and 105.3 ± 1.6 Ma. This is similar to published ages from plagioclase*
36 *xenocrysts in recent Barren Island volcanics, and in zircons from a gabbro sample from the*
37 *Andaman ophiolite, which we interpret as the age of the original ophiolite formation. The Ar/Ar*
38 *ages are considerably older than arc magmatic gabbros and plagiogranites of the overlying*
39 *ophiolite previously dated at 99-93 Ma and thought to reflect the ophiolite age, but recently re-*
40 *interpreted as a volcanic arc built on the ophiolite. Combined with ages of Woyla-Sundaland*
41 *collision we argue that subduction polarity reversal can take no longer than 6 My to be fully*
42 *effective.*

43

44 **1 Introduction**

45 The formation of new subduction zones is critical in the plate tectonic cycle. A fundamental way
46 in which new subduction zones form is through subduction polarity reversal following arc-
47 continent collision (e.g. Chemenda et al., 2001; Dewey, 1976; Faccenda et al., 2008; Pysklywec,
48 2001; Stern, 2004; Stern & Gerya, 2017) where upon ongoing convergence, the arrest of one
49 subduction zone is followed by the initiation of another, typically within or behind the older arc
50 (Fig. 1). The arrest of the older subduction zone is then often related to arrival of buoyant
51 continental, or thickened oceanic lithosphere on the original downgoing plate in the trench. For
52 instance, the arrival of the Ontong-Java oceanic plateau in the Vitiaz trench led to the formation
53 of the New Hebrides subduction zone in the Vitiaz/Melanesian arc (Hall, 2002; Knesel et al.,
54 2008). Subduction polarity reversal following arc-continent collision was also proposed in the
55 Aleutian arc (Vaes et al., 2019), or to form the modern Kamchatka subduction zone (Domeier et
56 al., 2017; Konstantinovskaia, 2001; Shapiro & Solov'ev, 2009; Vaes et al., 2019). Modern
57 examples where polarity reversal may be ongoing are the Banda arc in Timor (e.g. Breen et al.,
58 1989; Harris, 2006; Tate et al., 2015), Taiwan (Chemenda et al., 2001), or the Solomon arc
59 (Cooper & Taylor, 1985; Cooper & Taylor, 1987). Despite the widespread recognition of arc
60 polarity reversal in the geological record, the dynamics and longevity of the reversal process are
61 poorly known. The duration of polarity reversal, i.e. the time between a subduction stops upon
62 arc continent collision and the time at which the new subduction is fully developed (see Fig. 1) is
63 however not known from direct evidences. Estimating the kinematic history of the transition
64 requires a geological record that allows dating the arrest of the old subduction (ceasing of the
65 arc) and the beginning of the new one, which is challenging given the destructive nature of active
66 margins.

67

68 The ophiolitic sequence of the Andaman Islands in the eastern Indian Ocean, however,
69 may preserve such a record. The Andaman and Nicobar archipelago is located in the forearc of
70 the Sunda-Sumatra subduction zone (Fig. 2.a,b). It exposes a thrust sequence of variably-
71 depleted and chromitite-bearing peridotites. The peridotites are overlain by mafic magmatic
72 rocks, and underlain by a serpentinite-hosted *mélange* that contains sheared greenschist- and
73 amphibolite-facies blocks, as well as radiolarian chert blocks with stratigraphic ages up to the
74 middle Eocene (Bandopadhyay & Carter, 2017a; Bandyopadhyay et al., 2020; Ghosh et al.,

75 2009, 2017; Ling et al., 1996; Sengupta et al., 1990). The ophiolitic rocks are unconformably
76 overlain by Paleocene to Eocene shallow-marine sandstones derived from a volcanic arc, and
77 after the middle Eocene the sequence thrust and tectonically repeated (Bandopadhyay &
78 Carter, 2017b).

79

80 The variably-depleted peridotites and the magmatic sequence of the ophiolites have long
81 been considered to represent one coherent, but tectonically dismembered suprasubduction zone
82 (SSZ) ophiolite sequence, (i.e. an ophiolite with an arc signature but with a structure of oceanic
83 lithosphere; Pearce et al., 1984; Stern, 2004 ; for the Andaman ophiolite see : Ghosh et al., 2009;
84 Pal, 2011; Pedersen et al., 2010). Magmatic rocks in the sequence include in places
85 plagiogranites (trondhjemites) and are overlain by Upper Cretaceous (Campanian) radiolarian
86 cherts (Ling et al., 1996). Two zircon U/Pb ages of these trondhjemites of 93.6 ± 1.3 Ma (Sarma
87 et al., 2010) and 95 ± 2 Ma (Pedersen et al., 2010) were interpreted to represent the formation of
88 Andaman ophiolite crust above a subduction zone. Whereas Pedersen et al., (2010) interpret
89 them to represent subduction initiation, others authors argue a geochemical signature typical of a
90 mature arc rather than a SSZ forearc setting (Jafri et al., 1995; Sarma et al., 2010). Near
91 Chiriyatapu, trondhjemites are found as blocks in an andesitic agglomerate. The agglomerates
92 have an arc signature (Bandyopadhyay et al., sub.) and are generally found overlying the
93 ophiolite. The absence or really minor presence of any other ophiolitic clasts (i.e. basalt,
94 peridotite), and their geochemical similarity to the andesitic components rather suggest that they
95 are cogenetic with the andesites (Bandyopadhyay et al., sub.). Bandyopadhyay et al. (sub.)
96 present new U/Pb dating of zircon from plagiogranites and gabbros (presumably formed in an arc
97 environment) from different parts of Andaman Island that yield ages of ~99 and ~93 Ma. In
98 addition the gabbro (SA-GAB1) yielded mixed ages between 105 and 98 Ma suggesting an
99 older, 105 Ma component inherited in a ~98 Ma melt (Bandyopadhyay et al., sub.). Combined,
100 these data show that there has been at least 5 Myr of magmatism with a diverse geochemical
101 signature suggesting an arc setting for parts of the Andaman ophiolites. Finally, thin ash layers
102 within Upper Cretaceous radiolarian cherts that intercalate with pillow lavas of South Andaman
103 also suggest that there was explosive volcanism during or not long after the magmatic sequence
104 of the ophiolite formed (Jafri et al., 2006).

105 Both the 5 Myr age range, as well as the broad range of geochemical signature and
106 composition of the volcanics of the Andaman Ophiolite are surprising (Ghosh et al., 2017).
107 Suprasubduction zone ophiolites are typically found in forearc settings where they form during
108 incipient upper plate extension following subduction initiation (e.g. Guilmette et al., 2018; Stern
109 et al., 2012). Mature volcanic arcs occur at a distance of typically ~100-300 km away from the
110 trench (Dickinson, 1973) with an average around 166 ± 66 km (Gill, 1981) or between 180 and
111 275 km (Syracuse & Abers, 2006). The juxtaposition of the SSZ forearc and arc may thus require
112 tectonic motion from a forearc to a back-arc domain, or that SSZ spreading occurred within a
113 mature arc setting. In the relatively restricted area of the Andaman Islands (350 x 40 km), it is
114 surprising to find a 5 Myr duration at least for magmatism since already formed crust moves at
115 half-spreading rate from the spreading centres. Typical magmatic spreading rates are of several
116 tens of km/Myr. It means that the ages of magmatic rocks in narrow ophiolite bodies like on
117 Andaman are typically within 1-2 Myr (e.g. in Oman: Rioux et al., 2016, 2013 or Turkey: van
118 Hinsbergen et al., 2016 and reference therein; Parlak et al., 2019). Instead, the minimal 5 Myr
119 transition between SSZ and arc magmatism that are found within a few metre in Andaman
120 suggests a more or less stationary magma source after the SSZ ophiolite is formed. After it
121 formed around 93 Ma, the arc is believed to be active at least until the Palaeocene to Eocene as
122 attested by arc-derived sandstone (Bandopadhyay, 2012)

123 Advokaat et al. (2018) recently suggested that when corrected for post-Cretaceous
124 tectonic motion along the Sunda forearc, the Andaman ophiolites restore adjacent to and west of
125 the extinct intra-oceanic Woyla arc that is now located on Sumatra and west-Java. This arc
126 collided with the Sundaland margin in the late Cretaceous. Advokaat et al. (2018) postulated that
127 the Andaman SSZ ophiolites may have formed during a subduction polarity reversal within or
128 adjacent to the Woyla arc upon its collision with Sundaland. In this paper, we study sheared
129 amphibolites below the Andaman ophiolite that are interpreted as their metamorphic sole (Pal &
130 Bhattacharya, 2010). Metamorphic soles are slivers of oceanic crust stripped of the downgoing
131 slab that are formed and underplated beneath the mantle wedge during subduction infancy. They
132 form during subduction initiation (Wakabayashi & Dilek, 2000) over a short time span (typically
133 of 1-2 My) and cool coevally to the formation of SSZ ophiolite (Hacker, 1994; Rioux et al.,
134 2016). Worldwide, they share very similar characteristic: they are formed in a warm thermal
135 regime, up to melting condition (850°C and 1.2 Gpa), in a much higher thermal regime than

136 expected for a mature subduction zone (Agard et al., 2016; Dubacq et al., 2019; Jamieson, 1986;
137 Soret et al., 2017; Wakabayashi & Dilek, 2003; Woodcock & Robertson, 1977). They commonly
138 have a 10-500 metre thickness in total and parts with different peak metamorphic grades
139 represent different tectonic slices. The higher temperature part of the sole are made of mafic
140 oceanic crust. The lower parts tend to show an increase of a sedimentary component (Casey &
141 Dewey, 1984). Cooling ages of metamorphic soles (i.e. obtained by the Ar/Ar method on
142 amphibole) are globally strongly correlated to the age of the crust of the overlying SSZ
143 ophiolites, suggesting that decompression and exhumation of soles are the result of upper plate
144 spreading (Dewey & Casey, 2013; van Hinsbergen et al., 2015). Such cooling ages may thus
145 serve as a proxy for the age of the SSZ ophiolite spreading (or hyper-extension). However they
146 provide only a minimum age for the initiation of subduction, which may predate SSZ spreading
147 by ~10 Myr or more as recently shown by Lu-Hf garnet ages in soles (Guilmette et al., 2018;
148 Pourteau et al., 2019).

149 The metamorphic sole are found below the ophiolites on Middle and North Andaman
150 Islands (Fig. 2a,b,c). We establish the pressure-temperature (PT) condition at which they formed
151 using empirical thermobarometry and pseudosection modelling. We provide Ar/Ar ages to
152 establish their cooling as proxy for the timing of SSZ ophiolite formation. We finally discuss our
153 results in terms of temporal and spatial relationships between SSZ ophiolite evolution, magmatic
154 evolution, and subduction polarity reversal dynamics.

155

156 **2 Geological setting**

157 2.1 Regional setting of the Andaman-Nicobar Islands

158 The Andaman and Nicobar Islands are located at the northernmost extension of the present-day
159 Sunda-Sumatra subduction system where the Indo-Australian plate is subducting below Eurasia
160 (Fig. 2a; Curray, 2005, 1989; McCaffrey, 1992, 2009). To the East of the Andaman and Nicobar
161 Islands is the Andaman Sea, a ~N-S spreading, Neogene pull-apart basin that formed in the back-
162 arc region of the Andaman subduction zone as a result of formation of the Burma-Andaman
163 forearc sliver, partitioning highly oblique India-Sundaland convergence over a trench in the west
164 and a transform system in the east (Curray, 2005). Restoring the opening of this basin brings the
165 Cretaceous-Paleogene rock record of the Andaman Islands towards the south, juxtaposed in
166 Oligocene time against west Sumatra (Curray, 2005).

167 On west Sumatra lies the accreted, formerly intra-oceanic Woyla volcanic arc. This arc
168 formed in earliest Cretaceous time within the Neotethys ocean (Hall, 2012). Paleomagnetic data
169 from the Woyla arc give paleolatitudes that are consistent with the arc having formed on the
170 Australian plate that until the Eocene moved eastwards relative to Eurasia (Advokaat et al.,
171 2018). Mid-late Cretaceous collision of the Woyla arc with Sundaland may have occurred
172 diachronously from north to south, and ongoing Australia-Eurasia motion likely triggered a
173 subduction polarity reversal recorded in the Indo-Myanmar and Andaman ophiolites (Advokaat
174 et al., 2018).

175 Regionally, remnants of oceanic lithosphere are preserved as ophiolite, generally
176 described as tectonically dismembered along the Indo-Myanmar suture zone (Fareeduddin &
177 Dilek, 2015; Liu et al., 2016; Singh et al., 2017). The Andaman Ophiolites are arguably the most
178 complete in the sense that ultramafic and mafic sequences are present (Ghosh et al., 2014, 2017;
179 Pal, 2011; Pal et al., 2003), although as described above, these may not, or not entirely, be
180 cogenetic (Bandyopadhyay et al., sub.). Metamorphic rocks were described from the
181 serpentinite-hosted sub-ophiolitic mélange and were suggested to reflect parts of a dismembered
182 metamorphic sole (Pal & Bhattacharya, 2010), but their precise metamorphic conditions, or the
183 age of formation and/or cooling, are so far unconstrained.

184

185 2.2 The Andaman Ophiolite

186 The tectonostratigraphy of the Andaman Islands has been discussed in detail in Bandopadhyay
187 (2012). The ophiolite contains a coherent mantle sequence mainly made of variably serpentinized
188 peridotite (tectonized harzburgite or lherzolite with chromitite and dunite pods) with in places
189 layered gabbros with local plagiogranite intrusions (Ghosh et al., 2014, 2017; Jafri et al., 1995;
190 Pal, 2011; Saha et al., 2010). Ophiolitic rocks crop out well along the Eastern shore line of
191 Rutland Island, South, Middle and North Andaman Islands (Fig. 2b). Plagiogranite from South
192 Andaman yielded the 93.6 ± 1.3 Ma U/Pb zircon age mentioned above (Sarma et al., 2010), and
193 the 95 ± 2 Ma U/Pb age (Pederson et al., 2010). In South Andaman, volcanic and volcanoclastic
194 rocks are divided in two groups based on field disposition and geochemical characters (Pillow
195 lava and East coast volcanics after Ray, 1985; Ray et al., 1988) made of basalt and andesite with
196 local felsic differentiates. The rocks of the crustal section show a progressive evolution from a
197 mid ocean ridge to SSZ affinity (Ghosh et al., 2017). The East Coast volcanics, reported from

198 South Andaman are cogenetic with gabbro from the Moho transition zone and have an arc
199 affinity (Bandyopadhyay et al., sub.; Ghosh et al., 2014). On top of the sequence are found some
200 hemipelagic sediments interbedded with basaltic layers. The sequence is assigned to the Upper
201 Cretaceous on the basis of fossil assemblages (Ling et al., 1996; Ling & Srinivasan, 1993; Pal et
202 al., 2003; Roy et al., 1988). Also, middle Eocene radiolarian cherts are found, in an isolated
203 outcrop in southern South Andaman (Ling et al., 1996; Ling & Srinivasan, 1993). Because the
204 Eocene sediments above the Andaman ophiolites are shallow-marine volcanic arc-derived
205 sandstones (Bandyopadhyay & Carter, 2017), there are likely part of the accretionary mélangé
206 underneath the ophiolite. Following the accretion of the youngest, Eocene, radiolarian chert to
207 the mélangé, the ophiolite and overlying forearc sediments were thrust and tectonically
208 repeated (Pal et al., 2003). This may coincide with the underthrusting of a seismically imaged
209 crustal block of possibly continental composition currently residing in the crust below the
210 Andaman ophiolite (Ghosh et al., 2017; Ratheesh Kumar et al., 2013; Singh et al., 2013).

211

212 2.3 The Andaman Islands metamorphic sole

213 The metamorphic rocks of the Andaman Islands have been investigated by Pal and Bhattacharya
214 (2010). They described two main localities in North and Middle Andaman. In north Andaman,
215 the metamorphic rocks are described as isolated small bodies below tectonized peridotite. In
216 Middle Andaman they are described as allochthonous bodies within the mélangé unit. The
217 localities are characterised by metabasites and metasediments, both described as metamorphosed
218 in the greenschist facies (Pal & Bhattacharya, 2010), but the metamorphic grade has not been
219 evaluated quantitatively. Geochemistry of the metabasites gives an alkaline basalt protolith and
220 the timing of formation was bracketed between the Cretaceous and the Oligocene (Pal &
221 Bhattacharya, 2010). Geochemically, the sole rocks show an island arc basalt to back-arc basin
222 basalts affinity (Bandyopadhyay et al., sub.). Sample AN1703 that is a quartz rich sample
223 interpreted to be a metachert has also an arc influence.

224

225 **3 Field observations, sampling and petrography**

226 3.1. Field observation and sampling

227 Strongly foliated and sheared greenschist- to amphibolite-facies rocks are found along the
228 eastern coast of Middle Andaman in the region of Panchawati RV (Fig. 2c). Apart from one in-
229 situ location where foliated amphibolites are found welded to basal peridotites of the ophiolite
230 (Fig. 2c,d and Table 1) these rocks occur as large, angular, loose boulders on the beach with
231 sizes up to 10 meters or more, suggesting they were likely not displaced over large distances.
232 These metamorphic blocks are found along a ~3 km long strip of beach. Far away (1 km) from
233 the in-situ location, the blocks decrease in size to pebbles and cobbles. The metamorphic rocks
234 are dominated by dark layered mafic amphibolite with feldspar, amphibole and clinopyroxene.
235 Sometimes late epidote is visible with the naked eye. The foliation is well defined, but mineral
236 lineation is not obvious probably due to the scattered recrystallization of amphibole. The
237 foliation is cross-cut by late mineral filling in brittle cracks (Fig. 2d). We also observed
238 greenschist-facies rocks that occur along shore (Fig. 2c). They consist in the field of coherent,
239 tens of meter sized blocks with metacherts interbedded with greenschist-facies metavolcanics
240 (Fig. 2d). We also investigated the Kalighat location on North Andaman previously described by
241 Pal and Bhattacharya, (2010). This locality shows 10 m sized blocks of metaquartzite and
242 phyllites outcropping in the jungle without clear relation to the surrounding ultramafic rocks. We
243 collected about 20 samples of the metamorphic sole and the above mélangé. Most of the samples
244 come from the main metamorphic sole locality along the coast of Middle Andaman (Fig. 2c;
245 Table 1).

246

247 3.2. Summary of microscopic observations

248 We here describe in detail the characteristic of our samples. As most samples are similar, we
249 provide a generic description. Specific description of samples analysed at the microprobe are
250 given in the Appendix S1. All samples were cut in the XZ plane of finite deformation except
251 when a penetrative deformation was not observable. In the last case, the samples were cut
252 perpendicular to the foliation.

253

254 Most of the amphibolite facies rocks have a nematoblastic texture. The foliation is defined by the
255 elongation of amphibole alternating with plagioclase. Green amphibole coexisting with
256 plagioclase constitute the dominant minerals (Fig. 3). We observed amphibole- and feldspar-rich

257 layers with a thickness varying from 0.1 to 5 mm between samples. In general the amphibole is
258 pristine, whereas the plagioclase often shows destabilization texture to a fine grained mixture of
259 epidote and albite (Fig. 3m). We found clinopyroxene in three samples (Fig. 3b,d,j,k,n,o; Table
260 1). It occurs as relict grains partially replaced by amphibole and indicates a peak metamorphic
261 assemblage composed of clinopyroxene + amphibole + plagioclase + a Ti-bearing phase. We
262 also observed inclusion of amphibole in clinopyroxene emphasizing their coexistence (Fig. 3d).
263 Titanium-bearing phases (titanite, rutile and ilmenite) are present as accessory minerals in all
264 samples (Fig. 3). They show complex relations (Fig. 3e,f,g,i,j,k,l) and detailed observation
265 (scanning electron microscope and reflected light) show that rutile is generally the first phase to
266 crystalize. It is overgrown / rimmed by ilmenite (Fig. 3i) and/or titanite (Fig. 3f,g,j,l). In most
267 samples we find rutile present as inclusion within titanite. We interpret the rutile to represent the
268 peak metamorphism condition. In some cases, rutile coexists with ilmenite (for example in
269 sample An1709a). In a few samples, we found epidote present as late crystals (Table 1). Apatite,
270 chlorite, and pyrite are minor component of some samples (Table 1). In addition, our samples
271 show late-stage (possibly hydrothermal) alteration features, with adularia (Fig. 3h) and calcite in
272 cross-cutting veins. Epidote and green amphibole also grow in such veins (Fig. 3b,h).

273 Greenschist facies rocks are made of green amphibole, plagioclase and epidote (Table 1).
274 Elongated light-green amphibole marks the foliation. Epidote is either present as porphyroblast
275 within the foliation or as layers marking the foliation. It is at textural equilibrium with
276 plagioclase and amphibole. Quartz-rich samples share the same mineral assemblage but have a
277 different texture. In places, we observed chlorite growing together with the above-mentioned
278 minerals. In all samples, late calcite or adularia veins cross-cut the main fabric, similar to the
279 amphibolite facies rocks. The Ti-bearing phase is either rutile overgrown by titanite, or only
280 titanite.

281 We also collected two sample from the Kalighat area in North Andaman previously
282 described by (Pal & Bhattacharya, 2010). They consist of quartz, white mica, epidote and opaque
283 minerals. The samples exhibit a foliation marked by the elongation of white mica flakes. We did
284 not investigate them more than under the microscope due to the lack of critical mineral
285 assemblages, and to the poor outcropping context.

286

287 **4 Methods, mineral chemistry and age determination**

288 To determine the PT conditions of formation of the metamorphic sole using
289 pseudosection modelling, we needed first to study the samples under the microscope. We then
290 collected chemical data for each mineral (mainly clinopyroxene, amphibole, feldspar). We
291 present below a compilation of our petrological study that is also summarized on Fig. 4. We then
292 summarize the chemical data obtained for the investigated samples.

293

294 4.1 Methods

295 Microprobe analyses were performed with both Cameca SXFive, SX 100 and a JEOL
296 Electron probe microanalyzer at CAMPARIS (Sorbonne Université, Paris) and GEOLAB
297 (Utrecht University) respectively. In all cases, we adopted classical analytical conditions (15 kV
298 acceleration voltage, 10 nA beam current, 3 μm beam size) wavelength-dispersive spectroscopy
299 mode). For calibration we used diopside (Ca,Mg,Si), orthoclase (K,Al), FeO (Fe), albite (Na),
300 Cr₂O₃ (Cr) and MnTiO₃ (Mn, Ti) in Paris, and Albite (Si,Al), Jadeite (Na), TiO (Ti), Adularia
301 (K), Diopside (Ca), Forsterite (Mg), Hematite (Fe), Tephroite (Mn), and Cr₂O₃, (Cr) in Utrecht.

302

303 Whole rock composition (major and trace elements) were obtained for five samples. All
304 samples were analysed at Actlabs (Canada) using their standard procedures (available online at
305 <https://actlabs.com/geochemistry/lithochem-and-whole-rock-analysis/lithochem/>
306 ; last accessed on the 13/12/2019).

307

308 We selected two amphibole-bearing samples for Ar/Ar determination. The two samples
309 were crushed and sieved to obtain 180 – 250 μm fractions. The finer particles were decanted off
310 in tap water and the coarser residue further ultrasonically washed in acetone and deionized water
311 several times. The optically best grains, void of any coatings, were handpicked under a
312 stereomicroscope. The samples were packed in aluminum capsules together with the Taylor
313 Creek Rhyolite flux monitor standard along with zero age reagent grade K₂SO₄ and optical grade
314 CaF₂ salts for interference corrections. The samples were irradiated at Institutt for Energiteknikk,
315 Kjeller, Norway for *ca.* 88.5 hours, with a nominal neutron flux density of *ca.* $1.3 \times 10^{13} \text{ n}^*(\text{cm}^{-2}$
316 $^*\text{s}^{-1})$. The interference correction factors for the production of isotopes from Ca and K are
317 located in the Appendix S2. Samples were placed in a 3.5 mm pit size aluminum sample disk and

318 step heated using a defocused 3.5 mm CO₂ laser beam from Photon Machine Fusions 10.6 with a
 319 flat energy spectrum. The extracted gases from the sample cell were expanded into a Piston Free
 320 Stirling Cryocooler, held at -130 °C, for trapping potential water vapor and further into a two-
 321 stage low volume extraction line (*ca.* 300 cm³), both stages equipped with SAES GP-50 (st101
 322 alloy) getters, the first running hot (*ca.* 350 °C) and the second running cold. The gas was
 323 analyzed with a MAP 215–50 mass spectrometer in static mode, installed at the Geological
 324 Survey of Norway. The peaks and baseline (AMU = 36.2) were determined during peak hopping
 325 for 10 cycles (15 integrations per cycle, 30 integrations on mass ³⁶Ar) on the different masses (⁴¹-
 326 ³⁵AMU) on a Balzers SEV 217 electron multiplier in analogue mode and regressed back to zero
 327 inlet time. Blanks were analyzed every third measurement. After blank correction, a correction
 328 for mass fractionation, ³⁷Ar and ³⁹Ar decay and neutron-induced interference reactions produced
 329 in the reactor was undertaken using in-house software AgeMonster, written by M. Ganerød. It
 330 implements the equations of McDougall and Harrison, (1999) and the newly proposed decay
 331 constant for ⁴⁰K after Renne et al. (2010). A ⁴⁰Ar/³⁶Ar ratio of 298.56 ± 0.31 from Lee et al.
 332 (2006), was used for the atmospheric argon correction and mass discrimination calculation using
 333 a power law distribution of the masses. We calculated J-values relative to an age of 28.619 ±
 334 0.036 Ma for the Taylor Creek Rhyolite sanidine flux monitor (Renne et al., 2010). We define a
 335 plateau according to the following requirements: at least three consecutive steps overlapping at
 336 the 95% confidence level (1.96σ) using the strict test: *overlap if: abs(age_n - age_{n+1}) <*
 337 *1.96√(σ_n² + σ_{n+1}²)* (if errors quoted at 1σ), ≥ 50% cumulative ³⁹Ar released, and mean square
 338 of weighted deviates (MSWD) less than the two tailed student T critical test statistics for n - 1.
 339 Weighted mean ages are calculated by weighting on the inverse of the analytical variance. The
 340 uncertainties are expanded in cases where MSWD > 1 using $\sigma * \sqrt{MSWD}$ to account for this
 341 excess error contribution.

342

343 4.2 Mineral chemistry

344 The composition of the minerals that we observed in thin sections reported below and
 345 representative analysis are given in Table 2. The full dataset is published online (Plunder et al.,
 346 2020)

347

348

349 Amphibole: The composition of the amphibole crystals defining the main fabric is generally
 350 calcic, between magnesio- and tschermakitic-hornblende following the classification of Leake et
 351 al. (1997). The late overgrowth plots in the actinolite field and some intermediate composition
 352 were also found (Fig. 4a,b). The Si content per formula unit (a.p.f.u.) varies between 6 and 8
 353 (hornblende and actinolite respectively). The XMg (with $\text{XMg} = \text{Mg}/[\text{Mg} + \text{Fe}^{2+}]$) is generally
 354 between 0.6 to 0.8. The analysis of a Ti vs. Si diagram shows a decreasing trend with relation to
 355 the textural site of the amphibole. The Ti a.p.f.u. content varies between 0.12 in hornblende to 0
 356 in actinolite and $[\text{Na} + \text{K}]^{\text{A}}$ varies from 0.6 to 0.

357

358 Clinopyroxene: Clinopyroxene has a diopside composition and shows differences in between
 359 samples (Fig. 4d). The average XMg (with $\text{XMg} = \text{Mg}/[\text{Mg} + \text{Fe}^{2+}]$) is 0.80 for sample AN1709a,
 360 0.64 for sample AN1709e, and 0.84 for sample AN1704a. The Na a.p.f.u. is on average 0.04 for
 361 samples AN1704a and AN1709a, 0.07 for sample AN1709e. We observed small intra sample
 362 variation in the order of ± 0.02 to ± 0.04 for the XMg and of ± 0.02 to ± 0.04 Na a.p.f.u. (Table 2).

363

364 Feldspar: All the primary feldspars are plagioclase (Fig. 4c). They have a composition ranging
 365 from Xanorthite=0 to Xanorthite=20 plotting in the field of albite to oligoclase. The late feldspar
 366 are classified as potassic feldspar, being identified as adularia with a formula unit very close to
 367 the end member (KAlSi_3O_8 ; Fig. 3c), a common mineral developing during episodes of
 368 hydrothermalism/fluid circulation at shallow levels (Cerny & Chapman, 1986)

369

370 Ti-bearing phases: when measured rutile or ilmenite show composition close to the pure end-
 371 members with formula unit close to TiO_2 and FeTiO_3 .

372

373 4.3 Ar/Ar ages

374 The main results and the degassing spectra can be found in Table 3 and Fig. 5, respectively. The
 375 raw analytical mass spectrometer output (following data reporting norms of Renne et al. (2010)
 376 are given in the online dataset (Plunder et al., 2020). The step heating experiments of
 377 Amphiboles from sample AN1704A and AN1709A (Fig. 5.a,b) reveal overlapping step ages of
 378 parts of the spectrum, defining inverse variance weighted plateau ages of 106.4 ± 2.1 Ma and
 379 105.3 ± 1.6 Ma respectively. These ages are within error of each other (Table 3). We interpret
 380 the plateau dates as reliable estimators of the cooling age of the metamorphic sole below ~450-

381 550°C (i.e. the closure temperature of the Ar/Ar system in hornblende; Baldwin et al., 1990;
382 Harrison, 1982).

383 **5 Thermobarometry**

384 6.1 Amphibole plagioclase thermometry and barometry

385 We determined the crystallization temperature of hornblende and plagioclase pairs using the
386 empirical thermometer of Holland and Blundy (1994). Since the plagioclase is often destabilized
387 in our samples, we only took the analyses with Xanorthite > 0.10 and a clear textural equilibrium
388 relation with the amphibole (e.g. pairs we measured together at the microprobe). For amphibole
389 we used the highest Ti content we measured (~0.06 to 0.08 Ti a.p.f.u; Fig. 4a) as it is interpreted
390 to increase with temperature (Ernst & Liu, 1998). When performing the thermometry we first set
391 the pressure to 0.8 GPa. This is a rather conservative assumption since the reaction is almost
392 entirely dependent on temperature. We then calculated the pressure using the calcic amphibole
393 barometer of Molina et al. (2015). We retrieved pressure between 0.6 and 0.9 GPa (Fig. 6a).
394 Using the calculated pressure we used an iterative scheme to refine the temperature. We obtained
395 temperatures between 600°C and 690°C from equation 1 (edenite + 4 quartz = tremolite + albite)
396 and between 630°C and 680°C from equation 2 (edenite + albite = richterite + anorthite) with
397 pressure range between 0.6 and 0.9 GPa (Fig. 6a). The difference with imposed pressure stays
398 within *ca.* 60°C and our result are coherent with previous estimates for similar paragenesis (Soret
399 et al., 2017).

400

401 5.2 Pseudosection modelling

402 One problem of pseudosection modelling with high variance rocks is to evaluate the amount of
403 water and the degree of oxidation of the rock. We calculated different pseudosection (i.e. a phase
404 diagram for a fixed bulk composition) using an updated version of the THERIAK-DOMINO software
405 package (de Capitani & Brown, 1987; de Capitani & Petrakakis, 2010; Jørgensen et al., 2019;
406 available on D. Tinkham's website <http://dtinkham.net/peq.html>, last accessed on April 15th
407 2019). For all calculations we used the tc62 database of Holland and Powell (2011) with the
408 following activity-composition relation: amphibole, clinopyroxene and melt (Green et al., 2016),
409 garnet, orthopyroxene, ilmenite, biotite (White et al., 2014), epidote (Holland & Powell, 2011),
410 spinel (White et al., 2002), and plagioclase (Holland & Powell, 2003). We selected sample
411 AN1709a for further thermobarometric investigation for two main reasons. First, it has reduced

412 variance due to the presence of clinopyroxene, making the assemblage more restrictive. Second,
413 it comes from an in-situ location. Using value reported in the literature for similar amphibolite
414 we arbitrary fixed values of XFe^{3+} to 0.12, 0.19 and 0.25 (with $XFe^{3+} = Fe^{3+}/[Fe^{3+} + Fe^{2+}]$).
415 These value of XFe^{3+} are similar to the range reported in Green et al. (2016) for the calibration of
416 the amphibole, clinopyroxene and melt models. We calculated multiple T-XH₂O diagram with
417 the fixed XFe^{3+} to investigate the water content. The XH₂O value varies from 0 to 1 (i.e. from
418 dry rock to excess water). It corresponds to a normalized variation of MH₂O = 0 to MH₂O = 7.41
419 mol % in the case of the modelled sample for $XFe^{3+} = 0.12$ (Table 4). When calculating a T-
420 XH₂O diagram, we set the pressure to 0.8 Gpa in agreement with our results from the amphibole-
421 plagioclase empirical thermometry and barometry.

422

423 For all calculations the solidus lies at conditions similar to what is shown in Palin et al.
424 (2016) for a MORB composition and the stable mineral assemblages are similar at first order.
425 The increase of the Fe^{3+} content has a minimal effect on its position except at low water content
426 where it shifts toward higher temperatures (See the position of the solidus line on the T-XH₂O
427 section of Fig. 6c-d). With $XFe^{3+} = 0.12$, the observed assemblage cannot be modelled
428 (amphibole + clinopyroxene + plagioclase + quartz + rutile + ilmenite; rutile is not predicted in
429 the diagram). A narrow field corresponding to the observed assemblage without rutile lies at
430 XH₂O between 0.45 and 0.5 with temperature varying between 550 and 800°C (Fig. 6b). With
431 increasing water content titanite becomes stable. We then calculated two PT pseudosection. We
432 assume the first one with XH₂O = 0.5 (i.e. that allows to compute an assemblage that is near to
433 the one observed) to represent near PT peak conditions where rutile and ilmenite are co-stable in
434 our sample. In the PT space, the observed assemblage appears in a relatively large field ranging
435 from 0.85 to 1.1 Gpa and between 600 and 725°C. It is limited towards high temperature by the
436 solidus, towards high pressure by the appearance of garnet and the destabilisation of ilmenite,
437 and towards low pressure by the destabilisation of rutile. The modal proportion of all phases is
438 close enough to what is observed in the samples (> 50% amphibole, 35 % plagioclase, 5-10 %
439 clinopyroxene, ~5%, rutile, ilmenite). We calculated a second pseudosection with a water
440 content corresponding on the measured loss on ignition (XH₂O = 0.6). In this calculation, the
441 solidus reaction shifts toward low temperature and lies around 650°C at 0.8 GPa. Neither rutile
442 nor ilmenite is predicted to be stable at supra solidus conditions except at pressure below 0.6

443 GPa where ilmenite is stable. We observe a field where titanite is stable together with amphibole,
 444 clinopyroxene, plagioclase and quartz. This corresponds to the observation from our thin section
 445 where titanite is overgrowing rutile and or rutile + ilmenite and is stable with amphibole,
 446 plagioclase and clinopyroxene.

447 With $X_{Fe^{3+}} = 0.19$ (Fig. 6c), the observed assemblage can be found at conditions where
 448 X_{H_2O} equals 0.47 at 675°C. We used the same approach as previously mentioned and calculated
 449 two PT pseudosection for $X_{H_2O} = 0.47$ and $X_{H_2O} = 0.6$ (i.e. the loss on ignition). On the first
 450 one, we observe the observed assemblage to lie in a field sharing the same topology as for the
 451 $X_{Fe^{3+}} = 0.12$ case, but with slightly lower pressure and temperature. With increasing water
 452 content, the PT pseudosection shares similarities as with the one calculated for $X_{Fe^{3+}} = 0.12$. The
 453 X_{Mg} of the modelled clinopyroxene increases to a value of 0.67. When increasing the Fe^{3+}
 454 content ($X_{Fe^{3+}} = 0.25$ case; Fig 6d), we observe very similar topologies either on the T- X_{H_2O}
 455 diagram or on the PT diagrams with different water quantity. The observed assemblage lies in a
 456 field that shifted to slightly lower pressure but higher temperature at 0.9 GPa and 700°C. We
 457 note that the chemistry of minerals tends to be more in agreement with the one observed in the
 458 case with $X_{Fe^{3+}} = 0.25$: the X_{Mg} modelled for clinopyroxene rises up to 0.7 in the pseudosection
 459 in contrast of the case with $X_{Fe^{3+}} = 0.12$ where $X_{Mg} = 0.65$. We calculated an additional PT
 460 pseudosection with $X_{Fe^{3+}} = 0.5$. The observed assemblage is modelled in a similar field, and the
 461 X_{Mg} the clinopyroxene rises up to 0.77 but the composition of the ilmenite solution model tends
 462 to be pure hematite excluding this case as a possibility for our PT estimates.

463 In any case, for the three $X_{Fe^{3+}}$ content, the observed assemblage lies at similar PT
 464 conditions of $675 \pm 50^\circ C$ and 0.9 ± 0.15 Gpa that we interpret to represent climax PT condition
 465 (Fig. 6 b-d). As in the case with $X_{Fe^{3+}} = 0.12$ the addition of water in the calculation allows to
 466 stabilize titanite together with clinopyroxene, amphibole and plagioclase. Considering the
 467 predicted composition of minerals, we take the case where the oxidation state is maximum
 468 ($X_{Fe^{3+}} = 0.25$) to be more representative of our rock, but we are aware that the PT condition
 469 computed for the observed assemblage do not change much with varying $X_{Fe^{3+}}$.

470

471 **6 Discussion**

472 **6.1 Condition of formation of the sole of the Andaman Islands**

473 In this study we constrained the condition of formation of the highest-grade metamorphic rocks
474 of the Andaman Islands using empirical thermobarometry and a pseudosection modelling. These
475 rocks formed at 0.9 GPa and 675°C. These results, and the single observation that the
476 amphibolites are welded to the peridotites of the Andaman Ophiolite, are coherent with
477 previously documented metamorphic soles around the world (e.g. Agard et al., 2016). The
478 samples we collected do not witness the highest-grade parts of soles reported elsewhere, (~850°C
479 and ~1.2 GPa; e.g. Agard et al., 2016; Cowan et al., 2014; Dubacq et al., 2019; Plunder et al.,
480 2016; Soret et al., 2017). This may either mean that these highest-grade parts were not accreted
481 in the Andaman case, (not all sole localities show the full sequence) or that it may be present
482 elsewhere below the Andaman ophiolite. However the calculated condition aligns well on the
483 typical warm geothermal gradient that is characteristic of subduction initiation ($> 20^{\circ}\text{C}/\text{km}$;
484 Casey & Dewey, 1984; Dewey & Casey, 2013; Hacker, 1990; Soret et al., 2017). The major
485 uncertainties on our PT estimates are related to the difficulty in estimating the water content and
486 the oxidation state of the rock. We have shown that even with large variation in the XFe^{3+} the PT
487 estimates are close and remains largely identical when one considers the uncertainties related to
488 the method. Interestingly, the XFe^{3+} variation does not affect the Ti-bearing phase relation much
489 (Soret et al., 2017). With increasing XFe^{3+} the PT condition of the observed assemblage shifts
490 slightly to higher temperature (+25°C) and to lower pressure (-0.1 GPa).

491
492 Interestingly, the variation of the water content has an important effect on the phase relation of
493 the Ti-bearing phases, especially for the rutile and or ilmenite-to-titanite transition. We may
494 argue on the basis of our observation and of our models that the water content has changed
495 during the evolutionary history of the rock. In our case, titanite-bearing paragenesis can only be
496 modelled for water content close to the loss on ignition (Fig. 6). On the opposite, the rutile-
497 ilmenite paragenesis can only be reproduced with quantities of water lower than the measured
498 loss on ignition. Titanite in our sample is observed as overgrowing rutile and clinopyroxene is
499 destabilized to amphibole. The addition of water in the clinopyroxene-bearing paragenesis could
500 produce a reaction consuming rutile or ilmenite and producing titanite instead (e.g. $\text{Cpx} + \text{Ilm/Rt}$
501 $+ \text{H}_2\text{O} \pm \text{Pl} = \text{Hbl} + \text{Ttn}$). The addition of water during the history of the rock is compatible with
502 the general subduction initiation context during which the mantle wedge registers a progressive
503 hydration (Prigent, et al., 2018a,b; Soret et al., 2016). Causes of such hydration of the exhuming

504 sole can be linked to the dehydration of later accreted metamorphic sole or dehydration/melting
505 of the sole at deeper level (Agard et al., 2018; Soret et al., 2017). It also means that such addition
506 of water needs to occur while the sole is exhuming. The PT condition at which this hydration
507 happened cannot be precisely constrained because the activity-composition model used here
508 being developed for relatively high temperature rocks (Green et al., 2016). We can, however,
509 eliminate the possibility that titanite developed during the late stages of hydrothermal activity
510 when adularia, carbonates, and actinolite crystallized (Fig. 3h). This is justified by the textural
511 relationship where titanite is stable with amphibole (Fig. 3f) or clinopyroxene (Fig. 3j,k).

512

513 6.2 Implication of the sole age: estimating the duration of flip polarity reversal

514 Our two plateau ages of 106.4 ± 2.1 Ma and 105.3 ± 1.6 Ma obtained for the metamorphic sole
515 are certainly older than the age of previously interpreted ophiolitic crust formation based on the
516 plagiogranite ages of 93-95 Ma (Pedersen et al., 2010; Sarma et al., 2010). The cooling ages of
517 the metamorphic sole obtained by the Ar/Ar method are systematically coeval with the
518 crystallization ages of the ophiolite (e.g. Oman: Hacker (1994); Turkey see review in van
519 Hinsbergen et al. (2016); Greece: Dimo-Lahite et al., 2001; Liati et al., 2004)). The inherited 105
520 Ma U/Pb component in one of the dated gabbro samples from the Andaman ophiolite
521 (Bandyopadhyay et al., sub.) may thus reflect the original SSZ crust onto which a 99-93 Ma arc
522 sequence was built. This age is also coeval with the 106 Ma Ar/Ar age on plagioclase xenocrysts
523 documented in recent lava flows of the Barren Island and is interpreted as the age of the
524 Andaman Ophiolite that are thought to be the basement of the Barren Island (Jyotiranjan S. Ray
525 et al., 2015).

526

527 In the light of the presented results and on data from the literature we propose the following,
528 revised scenario for the formation and evolution of the Andaman ophiolites and provide
529 estimates on the duration of a subduction polarity reversal that we interpret to be the result of the
530 Woyla-Sundaland arc-continent collision (Fig. 7).

531

532 1. By *ca.* 120 Ma the conceptual Ngalau plate was consumed in a double-verging
533 subduction system (Advokaat et al., 2018; Barber et al., 2005). This resulted in the
534 development of the intra oceanic Woyla arc and of the Western Sumatra arc on

535 Sundaland (Fig. 7a). This is attested by the 122-105 Ma ages of the volcanic rocks in the
536 Woyla arc (Gafoer et al., 1993; Koning, 1985), and the assemblage of Mid Jurassic to
537 Upper Cretaceous sediments and intrusive rocks in the Western Sumatra arc (Advokaat et
538 al., 2018; Barber et al., 2005; Zhang et al., 2019).

539 2. While the triple junction was moving, southwards, the Woyla arc or island arc generated
540 above the subduction zones collided with Eurasia. It leads to the southwards propagation
541 of subduction initiation towards the back-arc basin behind the Woyla arc (Fig. 7b). The
542 back arc basin is a good candidate for the propagation of the subduction zone as it
543 represents a global mechanical weakness where subduction can nucleate (e.g. Beaussier
544 et al., 2019, 2018). Whether the ridge itself or another structure/weakness is the place
545 where subduction initiates remains however speculative. Meanwhile arc volcanism
546 continued on both sides of the Ngalau plate (i.e. in the W. Sumatra and Woyla arcs)
547 showing that arc collision there was not underway yet.

548 3. We interpret the ~105 Ma Ar/Ar age on amphibole as a cooling age. It means that by
549 ~105 Ma the metamorphic sole of the Andaman Islands was exhuming (Fig.7 c). This is
550 coeval with the formation of SSZ gabbros documented in the Andaman ophiolite (i.e. the
551 ~105 Ma component of the U/Pb ages on zircon found in gabbros; Bandyopadhyay et al.,
552 sub.) and the ~106 Ma Ar/Ar age on plagioclase xenocrysts the Barren Island volcanic
553 rocks (Jyotiranjana S. Ray et al., 2015)). The Woyla arc and West-Sumatra arc enter their
554 final stages, but are still active (Gafoer et al., 1993; Koning, 1985; Zhang et al., 2019).

555 4. From 99 Ma onwards, a true magmatic arc became active above the newly formed NE
556 dipping subduction (Fig. 7d). This activity is attested by (i) 99-93 Ma plagiogranite with
557 an arc affinity intruding the ophiolite (Bandyopadhyay et al., sub.; Jafri et al., 1995;
558 Sarma et al., 2010) and (ii) by agglomerates (arc volcanic pyroclastic deposits) amongst
559 which some include 95 Ma plagiogranite components dated by Pedersen et al. (2010).
560 These ages are considerably younger than the cooling ages of the Andaman metamorphic
561 sole and demonstrate that the subduction was fully developed by that time (Fig. 7d). This
562 also implies that a significant part of magmatic and mantle rocks previously considered
563 as the Andaman ophiolite are actually the expression on an arc emplaced in the ophiolite
564 (Fig. 7d; Bandyopadhyay et al., sub). The Woyla arc is then accreted to Sundaland once
565 the Ngalau plate was entirely consumed (Fig. 7d; Advokaat et al., 2018). Magmatism on

566 the W. Sumatra arc occurs until at least 85 Ma in the southernmost part of (Zhang et al.,
567 2019) and could have stopped earlier to the north (Wang et al., 2014).

568

569 All in all, this scenario allows us to evaluate the duration of subduction polarity reversal in
570 context of the Woyla arc-Sundaland collision. We use the age of the sole likely representing
571 exhumation as a minimum age for subduction initiation. In other settings, sole exhumation ages
572 are coeval with the ages of SSZ ophiolite formation (Hacker, 1994; van Hinsbergen et al., 2015
573 and reference therein). In the case of the Andaman Islands, the age we obtained for the
574 metamorphic sole, is coeval with the ages documented in the ophiolite (105 Ma age component
575 in gabbros; Bandyopadhyay et al., sub). The formation of part of the present day ophiolite
576 occurred ~6 Myr prior to the formation of the 99-93 Ma new magmatic arc sequence that formed
577 in and on the ophiolite (Fig. 7d). This gives us a minimum 6 My duration for subduction polarity
578 reversal. However, it is reasonable to argue that subduction initiation must have predated the
579 cooling of the sole. The delay between prograde metamorphism dated using Lu-Hf ages on
580 garnet and exhumation ages documented by Ar/Ar ages on amphibole in other sole locations in
581 western Turkey and Oman (Guilmette et al., 2018; Pourteau et al., 2019) is as much as 8-12 Myr.
582 It means that subduction might have initiated as early as ca. 115 Ma on the Andaman transect.
583 Combining that with the minimum duration, it allows us to speculate that subduction reversal
584 occurs at least over a 14-18 My. This time span is consistent with timing proposed for other
585 subduction polarity reversals, such as 22 My documented from the sedimentary record in
586 Dominican Republic and Puerto Rico (in the Caribbean region; Lebron and Perfit, 1993), 10-22
587 My on the basis of geochronological data from the Irish Caledonides (Clift et al., 2003), 12 My
588 from the age of porphyry copper deposit in the South West Pacific (Solomon, 1990) and is in the
589 same range as the subduction polarity reversal documented below Taiwan (Clift et al., 2003; von
590 Hagke et al., 2016). From these examples, subduction polarity reversal may last tens of millions
591 year, depending most likely on the plate convergence rate and on the geometry of the plate
592 boundary system and the obliquity between the colliding arc and continent. Subduction polarity
593 reversal is likely to be a gradual, 3 dimensional process that takes tens of Myr on a given
594 transect. The Andaman Islands setting may thus provide a test case for thermomechanical
595 numerical model studies on the dynamics of subduction initiation through polarity reversal in
596 response to arc continent collision. Further test would be to .investigate the velocity of

597 subduction initiation propagation that Zhou et al. (2018) propose to be in the order of 10-20
598 cm/yr. and to test whether the ridge or other structures in the back-arc basin is the key location
599 for subduction initiation.

600 **7 Conclusions**

601 We here provide the estimation of the duration of a subduction polarity reversal during arc
602 continent collision that occurred during the Late Cretaceous. Using the case study of the
603 Andaman Islands, we constrained the timing of subduction initiation by a petrochronological
604 study of the metamorphic sole. The sole formed at 0.95 GPa and 675°C and was exhumed no
605 later than *ca.* 105 Ma as constrained by two new Ar/Ar ages on hornblende. The geochemistry of
606 the metamorphic sole fits with a back-arc basin origin close to the Woyla arc, when that collided
607 with Sundaland, in agreement with existing palaeogeographic reconstructions, an ideal place for
608 subduction initiation. Altogether, our petrochronological and field data together with literature
609 review advocates for a subduction polarity reversal following the diachronous collision of the
610 Woyla arc with Sundaland. We may estimate that subduction polarity reversal have occurred on
611 timescales of at least 6 Myr. The well-constrained Andaman Islands case study could serve for
612 further investigation of subduction polarity reversal as a fundamental mechanism to create new
613 subduction zones.

614

615 **Acknowledgments:** A.P., D.J.J.v.H., and E.L.A. were funded through ERC starting grant SINK
616 (306810) to D.J.J.v.H. D.J.J.v.H. acknowledges NWO Vici grant 865.17.001. DB acknowledges
617 the support of DST INSPIRE Fellowship (IF 130148). BG acknowledges financial support
618 received from Science and Engineering Research Board, DST, India (EMR/2017/000929). We
619 thank the Ramakrishna mission in Port-Blair for accommodation and Yael Engbers for help
620 during the fieldwork. We thank two anonymous reviewers and Osman Parlak for constructive
621 comments. We thank J. Geissman and Y. Eyüboğlu for editorial handling. We are indebted to
622 Loes van Unnik Hoorn, N. Rividi and M. Fialin at the Camparis service in Paris and to T. Bouten
623 and S. Maatvev at the Geolab in Utrecht for help during microprobe session. All raw probe data
624 are accessible at the following data repository:

625 https://figshare.com/articles/2019TC005762R_Raw_Probe_Data_xlsx/11890233.

626

627

629 References

- 630 Advokaat, E. L., Bongers, M. L. M., Rudyawan, A., BouDagher-Fadel, M. K., Langereis, C. G., & van Hinsbergen,
631 D. J. J. (2018). Early Cretaceous origin of the Woyla Arc (Sumatra, Indonesia) on the Australian plate. *Earth
632 and Planetary Science Letters*, 498, 348–361. <https://doi.org/10.1016/j.epsl.2018.07.001>
- 633 Agard, P., Yamato, P., Soret, M., Prigent, C., Guillot, S., Plunder, A., et al. (2016). Subduction infancy: mantle
634 resistance to slab penetration and metamorphic sole formation controlled by plate interface rheological
635 switches. *Earth and Planetary Science Letters*, 451, 208–220. <https://doi.org/10.1016/j.epsl.2016.06.054>
- 636 Agard, P., Plunder, A., Angiboust, S., Bonnet, G., & Ruh, J. (2018). The subduction plate interface: rock record and
637 mechanical coupling (from long to short timescales). *Lithos*, 320–321, 537–566.
638 <https://doi.org/10.1016/j.lithos.2018.09.029>
- 639 Baldwin, S. L., Harrison, T. M., & Fitz, G. J. D. (1990). Diffusion of (super 40) Ar in metamorphic hornblende.
640 *Contributions to Mineralogy and Petrology*, 105(6), 691–703. Retrieved from
641 <https://link.springer.com/article/10.1007/BF00306534>
- 642 Bandopadhyay, P. C. (2012). Re-interpretation of the age and environment of deposition of Paleogene turbidites in
643 the Andaman and Nicobar Islands, Western Sunda Arc. *Journal of Asian Earth Sciences*, 45, 126–137.
644 <https://doi.org/10.1016/j.jseaes.2011.08.018>
- 645 Bandopadhyay, P. C., & Carter, A. (2017a). Introduction to the geography and geomorphology of the Andaman–
646 Nicobar Islands. *Geological Society of London Memoir*, 47, 9–18.
- 647 Bandopadhyay, P. C., & Carter, A. (2017b). Submarine fan deposits: petrography and geochemistry of the Andaman
648 Flysch. *Geological Society of London Memoir*, 47, 133–140.
- 649 Bandyopadhyay, D., Ghosh, B., Guilmette, C., Plunder, A., Corfu, F., Advokaat, E. L., et al. (n.d.). Clue to the
650 Cretaceous subduction initiation in South-East Asia - A geochronological and geochemical perspective from
651 Andaman Ophiolite. *Geochemistry Geophysics Geosystems*.
- 652 Bandyopadhyay, D., van Hinsbergen, D. J. J., Plunder, A., Bandopadhyay, P. C., Advokaat, E. L., Morishita, T., &
653 Ghosh, B. (2020). Andaman Ophiolites: an overview. In J. S. Ray & M. Radhakrishna (Eds.), *The Andaman
654 Islands and Adjoining Offshore: Geology, Tectonics and Paleoclimate*. Springer Nature Switzerland AG 2020.
655 https://doi.org/https://doi.org/10.1007/978-3-030-39843-9_1
- 656 Barber, A. J., Crow, M. J., & De Smet, M. E. M. (2005). Chapter 14 Tectonic Evolution. *Geological Society,
657 London, Memoirs*, 31, 234–259.
- 658 Beaussier, S. J., Gerya, T. V., & Burg, J.-P. (2018). 3D numerical modelling of the Wilson cycle: structural
659 inheritance of alternating subduction polarity. *Geological Society, London, Special Publications*, SP470.15.
660 <https://doi.org/10.1144/sp470.15>
- 661 Beaussier, S. J., Gerya, T. V., & Burg, J. P. (2019). Near-ridge initiation of intraoceanic subduction: Effects of
662 inheritance in 3D numerical models of the Wilson Cycle. *Tectonophysics*, 763(November 2018), 1–13.
663 <https://doi.org/10.1016/j.tecto.2019.04.011>
- 664 Breen, N. A., Silver, E. A., & Roof, S. (1989). The Wetar Back Arc Thrust Belt, eastern Indonesia: The effect of
665 accretion against an irregularly shaped arc. *Tectonics*, 8(1), 85–98. <https://doi.org/10.1029/TC008i001p00085>
- 666 de Capitani, C., & Brown, T. H. (1987). The computation of chemical equilibrium in complex systems containing
667 non-ideal solutions. *Geochimica et Cosmochimica Acta*, 51, 2639–2652.
- 668 de Capitani, C., & Petrakakis, K. (2010). The computation of equilibrium assemblage diagrams with
669 Theriak/Domino software. *American Mineralogist*, 95(7), 1006–1016. <https://doi.org/10.2138/am.2010.3354>
- 670 Casey, J. F., & Dewey, J. F. (1984). Initiation of subduction zones along transform and accreting plate boundaries,
671 triple-junction evolution, and forearc spreading centres - implications for ophiolitic geology and obduction.
672 *Geological Society, London, Special Publications*, 13(v), 269–290.
673 <https://doi.org/10.1144/GSL.SP.1984.013.01.22>
- 674 Cerny, P., & Chapman, R. (1986). Adularia from hydrothermal vein deposits: extremes in structural state. *Canadian
675 Mineralogist*, 24(4), 717–728.
- 676 Chemenda, A. I., Yang, R.-K., Stephan, J.-F., Konstantinovskaya, E. A., & Ivanov, G. M. (2001). New results from
677 physical modelling of arc–continent collision in Taiwan: evolutionary model. *Tectonophysics*, 333(1–2), 159–
678 178. [https://doi.org/10.1016/S0040-1951\(00\)00273-0](https://doi.org/10.1016/S0040-1951(00)00273-0)
- 679 Clift, P. D., Schouten, H., & Draut, A. E. (2003). A general model of arc-continent collision and subduction polarity
680 reversal from Taiwan and the Irish Caledonides. *Geological Society, London, Special Publications*, 219(1),
681 81–98. <https://doi.org/10.1144/GSL.SP.2003.219.01.04>
- 682 Cooper, P., & Taylor, B. (1987). Seismotectonics of New Guinea: A model for arc reversal following arc-continent
683 collision. *Tectonics*, 6(1), 53–67.

- 684 Cooper, P. A., & Taylor, B. (1985). Polarity reversal in the Solomon Islands arc. *Nature*, 314(6010), 428–430.
685 <https://doi.org/10.1038/314428a0>
- 686 Cowan, R. J., Searle, M. P., & Waters, D. J. (2014). Structure of the metamorphic sole to the Oman Ophiolite,
687 Sumeini Window and Wadi Tayyin: implications for ophiolite obduction processes. *Geological Society,*
688 *London, Special Publications*, 392(1), 155–175. <https://doi.org/10.1144/SP392.8>
- 689 Curray, J. R. (1989). The Sunda arc: a model for oblique plate convergence. *Netherlands Journal of Sea Research*,
690 24, 131–140. Retrieved from <https://www.sciencedirect.com/science/article/pii/0077757989901440>
- 691 Curray, J. R. (2005). Tectonics and history of the Andaman Sea region. *Journal of Asian Earth Sciences*, 25(1),
692 187–232. <https://doi.org/10.1016/j.jseaes.2004.09.001>
- 693 Dewey, J.F. (1976). Ophiolite obduction. *Tectonophysics*, 31(1–2), 93–120. <https://doi.org/10.1016/0040->
694 1951(76)90169-4
- 695 Dewey, John F., & Casey, J. F. (2013). The sole of an ophiolite: the Ordovician Bay of Islands Complex,
696 Newfoundland. *Journal of the Geological Society, London*, 170(5), 715–722. <https://doi.org/10.1144/jgs2013->
697 017
- 698 Dickinson, W. R. (1973). Widths of modern arc-trench gaps proportional to past duration of igneous activity in
699 associated magmatic arcs. *Journal of Geophysical Research*, 78(17), 3376–3389.
700 <https://doi.org/10.1029/jb078i017p03376>
- 701 Dimo-Lahite, A., Monié, P., & Vergély, P. (2001). Metamorphic soles from the Albanian ophiolites: Petrology,
702 $40\text{Ar}/39\text{Ar}$ geochronology, and geodynamic evolution. *Tectonics*, 20(1), 78–96.
- 703 Domeier, M., Shephard, G. E., Jakob, J., Gaina, C., Doubrovine, P. V., & Torsvik, T. H. (2017). Intraoceanic
704 subduction spanned the Pacific in the Late Cretaceous–Paleocene. *Science Advances*, 3(11), 1–6.
705 <https://doi.org/10.1126/sciadv.aao2303>
- 706 Dubacq, B., Soret, M., Jewison, E., & Agard, P. (2019). Early subduction dynamics recorded by the metamorphic
707 sole of the Mt. Albert ophiolitic complex (Gaspé Quebec). *Lithos*, 334–335, 161–179.
708 <https://doi.org/10.1016/j.lithos.2019.03.019>
- 709 Ernst, W. G., & Liu, J. (1998). Experimental phase-equilibrium study of Al- and Ti-contents of calcic amphibole in
710 MORB — A semiquantitative thermobarometer. *American Mineralogist*, 83, 952–969.
- 711 Faccenda, M., Gerya, T. V., & Chakraborty, S. (2008). Styles of post-subduction collisional orogeny: Influence of
712 convergence velocity, crustal rheology and radiogenic heat production. *Lithos*, 103(1–2), 257–287.
713 <https://doi.org/10.1016/j.lithos.2007.09.009>
- 714 Fareeduddin, & Dilek, Y. (2015). Structure and petrology of the Nagaland-Manipur Hill Ophiolitic Mélange zone ,
715 NE India : A Fossil Tethyan Subduction Channel at the India – Burma Plate Boundary. *Episodes*, (December),
716 298–314. <https://doi.org/10.18814/epiiugs/2015/v38i4/82426>
- 717 Gafoer, S., Amin, T. C., & Pardede, R. (1993). Geology of the Bengkulu Quadrangle, Sumatra, scale 1: 250.000.
718 *Geological Research and Development Centre, Bandung*.
- 719 Ghosh, B., Pal, T., Bhattacharya, A., & Das, D. (2009). Petrogenetic implications of ophiolitic chromite from
720 Rutland Island, Andaman - A boninitic parentage in supra-subduction setting. *Mineralogy and Petrology*,
721 96(1–2), 59–70. <https://doi.org/10.1007/s00710-008-0039-9>
- 722 Ghosh, B., Morishita, T., Gupta, B. Sen, Tamura, A., Arai, S., & Bandyopadhyay, D. (2014). Moho transition zone
723 in the Cretaceous Andaman ophiolite, India: A passage from the mantle to the crust. *Lithos*, 198–199(1), 117–
724 128. <https://doi.org/10.1016/j.lithos.2014.03.027>
- 725 Ghosh, B., Bandyopadhyay, D., & Morishita, T. (2017). Chapter 7 Andaman–Nicobar Ophiolites, India: origin,
726 evolution and emplacement. *Geological Society, London, Memoirs*, 47(1), 95 LP – 110. Retrieved from
727 <http://mem.lyellcollection.org/content/47/1/95.abstract>
- 728 Gill, J. B. (1981). *Orogenic Andesites and Plate Tectonics* (Vol. 16). Berlin, Heidelberg: Springer Berlin
729 Heidelberg. <https://doi.org/10.1007/978-3-642-68012-0>
- 730 Green, E. C. R., White, R. W., Diener, J. F. A., Powell, R., Holland, T. J. B., & Palin, R. M. (2016). Activity–
731 composition relations for the calculation of partial melting equilibria for metabasic rocks. *Journal of*
732 *Metamorphic Geology*, 1–25. <https://doi.org/10.1017/CBO9781107415324.004>
- 733 Guilmette, C., Smit, M. A., van Hinsbergen, D. J. J., Gürer, D., Corfu, F., Charette, B., et al. (2018). Forced
734 subduction initiation recorded in the sole and crust of the Semail Ophiolite of Oman. *Nature Geoscience*,
735 11(9), 688–695. <https://doi.org/10.1038/s41561-018-0209-2>
- 736 Hacker, B. R. (1990). Simulation of the metamorphic and deformational history of the metamorphic sole of the
737 Oman Ophiolite. *Journal of Geophysical Research*, 95(B4), 4895. <https://doi.org/10.1029/JB095iB04p04895>
- 738 Hacker, B. R. (1994). Rapid emplacement of young oceanic lithosphere: argon geochronology of the Oman
739 ophiolite. *Science*, 265, 1563–1565. <https://doi.org/10.1126/science.265.5178.1563>

- 740 von Hagke, C., Philippon, M., Avouac, J. P., & Gurnis, M. (2016). Origin and time evolution of subduction polarity
741 reversal from plate kinematics of Southeast Asia. *Geology*, *44*(8), 659–662. <https://doi.org/10.1130/G37821.1>
- 742 Hall, R. (2002). Cenozoic geological and plate tectonic evolution of SE Asia and the SW Pacific: computer-based
743 reconstructions, model and animations. *Journal of Asian Earth Sciences*, *20*(4), 353–431.
744 [https://doi.org/10.1016/S1367-9120\(01\)00069-4](https://doi.org/10.1016/S1367-9120(01)00069-4)
- 745 Hall, R. (2012). Late Jurassic-Cenozoic reconstructions of the Indonesian region and the Indian Ocean.
746 *Tectonophysics*, *570–571*, 1–41. <https://doi.org/10.1016/j.tecto.2012.04.021>
- 747 Harris, R. (2006). Rise and fall of the Eastern Great Indonesian arc recorded by the assembly, dispersion and
748 accretion of the Banda Terrane, Timor. *Gondwana Research*, *10*(3–4), 207–231.
749 <https://doi.org/10.1016/J.GR.2006.05.010>
- 750 Harrison, M. T. (1982). Diffusion of ^{40}Ar in hornblende. *Contributions to Mineralogy and Petrology*, *78*(3), 324–
751 331. <https://doi.org/10.1007/BF00398927>
- 752 van Hinsbergen, D. J. J., Peters, K., Maffione, M., Spakman, W., Guilmette, C., Thieulot, C., et al. (2015).
753 Dynamics of intraoceanic subduction initiation: 2. Suprasubduction zone ophiolite formation and metamorphic
754 sole exhumation in context of absolute plate motions. *Geochemistry, Geophysics, Geosystems*, *16*(6), 1771–
755 1785. <https://doi.org/10.1002/2015GC005745>
- 756 van Hinsbergen, D. J. J., Maffione, M., Plunder, A., Kaymakçı, N., Ganerød, M., Hendriks, B. W. H., et al. (2016).
757 Tectonic evolution and paleogeography of the Kırşehir Block and the Central Anatolian Ophiolites, Turkey.
758 *Tectonics*, *35*, 983–1014. <https://doi.org/10.1002/2015TC004018>. Received
- 759 Holland, T., & Blundy, J. (1994). Non-ideal interactions in calcic amphiboles and their bearing on amphibole-
760 plagioclase thermometry. *Contributions to Mineralogy and Petrology*, *116*(4), 433–447. <https://doi.org/XCa>
- 761 Holland, T., & Powell, R. (2003). Activity-compositions relations for phases in petrological calculations: An
762 asymmetric multicomponent formulation. *Contributions to Mineralogy and Petrology*, *145*, 492–501.
763 <https://doi.org/10.1007/s00410-003-0464-z>
- 764 Holland, T. J. B., & Powell, R. (2011). An improved and extended internally consistent thermodynamic dataset for
765 phases of petrological interest, involving a new equation of state for solids. *Journal of Metamorphic Geology*,
766 *29*(3), 333–383. <https://doi.org/10.1111/j.1525-1314.2010.00923.x>
- 767 Jafri, S. H., Charan, S. N., & Govil, P. K. (1995). Plagiogranite from the Andaman ophiolite belt, Bay of Bengal,
768 India. *Journal of the Geological Society*, *152*(4), 681–687. <https://doi.org/10.1144/gsjgs.152.4.0681>
- 769 Jafri, S. H., Subba Rao, M. V., & Ramesh, S. L. (2006). Occurrence of ash beds in radiolarian cherts from South
770 Andaman Island, Bay of Bengal, India: Evidence for Late Cretaceous explosive volcanism. *Current Science*,
771 *91*(12), 1614–1615.
- 772 Jamieson, R. A. (1986). P-T paths from high temperature shear zones beneath ophiolites. *Journal of Metamorphic*
773 *Geology*, *4*(1), 3–22. <https://doi.org/10.1111/j.1525-1314.1986.tb00335.x>
- 774 Jørgensen, T. R. C., Tinkham, D. K., & Lesher, C. M. (2019). *Low-P and high-T metamorphism of basalts: Insights*
775 *from the Sudbury impact melt sheet aureole and thermodynamic modelling*. *Journal of Metamorphic Geology*
776 (Vol. 37). <https://doi.org/10.1111/jmg.12460>
- 777 Knesel, K. M., Cohen, B. E., Vasconcelos, P. M., & Thiede, D. S. (2008). Rapid change in drift of the Australian
778 plate records collision with Ontong Java plateau. *Nature*, *454*(7205), 754–7.
779 <https://doi.org/10.1038/nature07138>
- 780 Koning, T. (1985). Petroleum Geology of the Ombilin Intermontane Basin, West Sumatra. *Indonesian Petroleum*
781 *Association, 14th Annual Convention Proceedings, 1*, 117–137.
- 782 Konstantinovskaia, E. . (2001). Arc–continent collision and subduction reversal in the Cenozoic evolution of the
783 Northwest Pacific: an example from Kamchatka (NE Russia). *Tectonophysics*, *333*(1–2), 75–94.
784 [https://doi.org/10.1016/S0040-1951\(00\)00268-7](https://doi.org/10.1016/S0040-1951(00)00268-7)
- 785 Leake, B. E., Woolley, A. R., Arps, C. E. S., Birch, W., Gilbert, C., Grice, J., et al. (1997). Nomenclature of
786 amphiboles: report of the subcommittee on amphiboles of the international mineralogical association ,
787 commission on new minerals and mineral names. *European Journal of Mineralogy*, *9*, 623–6514.
- 788 Lebron, M. C., & Perfit, M. R. (1993). Stratigraphic and Petrochemical Data Support Subduction Polarity Reversal
789 of the Cretaceous Caribbean Island Arc. *The Journal of Geology*, *101*(3), 389–396.
790 <https://doi.org/10.1086/648231>
- 791 Lee, J.-Y., Marti, K., Severinghaus, J. P., Kawamura, K., Yoo, H.-S., Lee, J. B., & Kim, J. S. (2006). A
792 redetermination of the isotopic abundances of atmospheric Ar. *Geochimica et Cosmochimica Acta*, *70*(17),
793 4507–4512. <https://doi.org/10.1016/J.GCA.2006.06.1563>
- 794 Liati, A., Gebauer, D., & Fanning, C. M. (2004). The age of ophiolitic rocks of the Hellenides (Vourinos, Pindos,
795 Crete): First U-Pb ion microprobe (SHRIMP) zircon ages. *Chemical Geology*, *207*(3–4), 171–188.

- 796 <https://doi.org/10.1016/j.chemgeo.2004.02.010>
- 797 Lin, T.-H., Mitchell, A. H. G., Chung, S.-L., Tan, X.-B., Tang, J.-T., Oo, T., & Wu, F.-Y. (2019). Two parallel
798 magmatic belts with contrasting isotopic characteristics from southern Tibet to Myanmar: zircon U–Pb and Hf
799 isotopic constraints. *Journal of the Geological Society*, *176*(3), 574–587. <https://doi.org/10.1144/jgs2018-072>
- 800 Ling, H. Y., & Srinivasan, S. (1993). Significance of Eocene radiolaria from port Blair group of south Andaman
801 island, India. *Journal of the Paleontological Society of India*, *38*, 1–5.
- 802 Ling, H. Y., Chandra, R., & Karkare, S. G. (1996). Tectonic significance of Eocene and Cretaceous radiolaria from
803 South Andaman Island, northeast Indian Ocean. *Island Arc*, *5*(2), 166–179. <https://doi.org/10.1111/j.1440-1738.1996.tb00023.x>
- 804
- 805 Liu, C. Z., Chung, S. L., Wu, F. Y., Zhang, C., Xu, Y., Wang, J. G., et al. (2016). Tethyan suturing in Southeast
806 Asia: Zircon U–Pb and Hf–O isotopic constraints from Myanmar ophiolites. *Geology*, *44*(4), 311–314.
807 <https://doi.org/10.1130/G37342.1>
- 808 McCaffrey, R. (1992). Oblique plate convergence, slip vectors, and forearc deformation. *Journal of Geophysical*
809 *Research*, *97*(92), 8905–8915.
- 810 McCaffrey, R. (2009). The Tectonic Framework of the Sumatran Subduction Zone. *Annual Review of Earth and*
811 *Planetary Sciences*, *37*(1), 345–366. <https://doi.org/10.1146/annurev.earth.031208.100212>
- 812 McDougall, I., & Harrison, T. M. (1999). *Geochronology and Thermochronology by the ⁴⁰Ar/³⁹Ar Method* (2 nd).
813 Oxford: Oxford University Press.
- 814 Molina, J. F., Moreno, J. A., Castro, A., Rodríguez, C., & Fershtater, G. B. (2015). Calcic amphibole
815 thermobarometry in metamorphic and igneous rocks: New calibrations based on plagioclase/amphibole Al–Si
816 partitioning and amphibole/liquid Mg partitioning. *Lithos*, *232*, 286–305.
817 <https://doi.org/10.1016/j.lithos.2015.06.027>
- 818 Pal, T. (2011). Petrology and geochemistry of the Andaman ophiolite: melt–rock interaction in a suprasubduction-
819 zone setting. *Journal of the Geological Society*, *168*(4), 1031–1045. <https://doi.org/10.1144/0016-76492009-152>
- 820
- 821 Pal, T., & Bhattacharya, A. (2010). Greenschist-facies sub-ophiolitic metamorphic rocks of Andaman Islands,
822 Burma–Java subduction complex. *Journal of Asian Earth Sciences*, *39*(6), 804–814.
823 <https://doi.org/10.1016/j.jseaes.2010.05.017>
- 824 Pal, T., Chakraborty, P. P., Gupta, T. D., & Singh, C. D. (2003). Geodynamic evolution of the outer-arc–forearc belt
825 in the Andaman Islands, the central part of the Burma–Java subduction complex. *Geological Magazine*,
826 *140*(3), 289–307. <https://doi.org/10.1017/S0016756803007805>
- 827 Parlak, O., Dunkl, I., Karaođlan, F., Kusky, T. M., Zhang, C., Wang, L., et al. (2019). Rapid cooling history of a
828 Neotethyan ophiolite: Evidence for contemporaneous subduction initiation and metamorphic sole formation.
829 *Bulletin of the Geological Society of America*, *131*(11–12), 2011–2038. <https://doi.org/10.1130/B35040.1>
- 830 Pearce, J. a., Lippard, S. J., & Roberts, S. (1984). Characteristics and tectonic significance of supra-subduction zone
831 ophiolites. *Geological Society, London, Special Publications*, *16*(1), 77–94.
832 <https://doi.org/10.1144/GSL.SP.1984.016.01.06>
- 833 Pedersen, R. B., Searle, M. P., Carter, A., & Bandopadhyay, P. C. (2010). U–Pb zircon age of the Andaman
834 ophiolite: implications for the beginning of subduction beneath the Andaman–Sumatra arc. *Journal of the*
835 *Geological Society, London*, *167*, 1105–1112. <https://doi.org/10.1144/0016-76492009-151>
- 836 Plunder, A., Bandyopadhyay, D., Ganerød, M., Advokaat, E., Ghosh, B., Bandopadhyay, P., & van Hinsbergen, D.
837 (2020). Dataset associated to the paper: History of subduction polarity reversal during arc–continent collision:
838 constraints from the Andaman Ophiolite and its metamorphic sole.
839 <https://doi.org/10.6084/m9.figshare.11890233.v3>
- 840 Plunder, Alexis, Agard, P., Chopin, C., Soret, M., Okay, A. I., & Whitechurch, H. (2016). Metamorphic sole
841 formation, emplacement and blueschist facies overprint: Early subduction dynamics witnessed by western
842 Turkey ophiolites. *Terra Nova*, *28*, 329–339. <https://doi.org/10.1111/ter.12225>
- 843 Pourteau, A., Scherer, E. E., Schorn, S., Bast, R., Schmidt, A., & Ebert, L. (2019). Thermal evolution of an ancient
844 subduction interface revealed by Lu–Hf garnet geochronology, Halilbađı Complex (Anatolia). *Geoscience*
845 *Frontiers*, *10*, 127–148. <https://doi.org/https://doi.org/10.1016/j.gsf.2018.03.004>
- 846 Prigent, C., Guillot, S., Agard, P., & Ildefonse, B. (2018). Fluid-Assisted Deformation and Strain Localization in the
847 Cooling Mantle Wedge of a Young Subduction Zone (Semail Ophiolite). *Journal of Geophysical Research:*
848 *Solid Earth*, *123*(9), 7529–7549. <https://doi.org/10.1029/2018JB015492>
- 849 Prigent, C., Agard, P., Guillot, S., Godard, M., & Dubacq, B. (2018). Mantle wedge (de)formation during
850 subduction infancy: Evidence from the base of the semail ophiolitic mantle. *Journal of Petrology*, *59*(11),
851 2061–2092. <https://doi.org/10.1093/petrology/egy090>

- 852 Pysklywec, R. N. (2001). Evolution of subducting mantle lithosphere at a continental plate boundary. *Geophysical*
853 *Research Letters*, 28(23), 4399–4402. <https://doi.org/10.1029/2001GL013567>
- 854 Ratheesh Kumar, R. T., Windley, B. F., Rajesh, V. J., & Santosh, M. (2013). Elastic thickness structure of the
855 Andaman subduction zone: Implications for convergence of the Ninetyeast Ridge. *Journal of Asian Earth*
856 *Sciences*, 78, 291–300. <https://doi.org/10.1016/j.jseas.2013.01.018>
- 857 Ray, Jyotiranjana S., Pande, K., & Bhutani, R. (2015). $^{40}\text{Ar}/^{39}\text{Ar}$ geochronology of subaerial lava flows of Barren
858 Island volcano and the deep crust beneath the Andaman Island Arc, Burma Microplate. *Bulletin of*
859 *Volcanology*, 77(6). <https://doi.org/10.1007/s00445-015-0944-9>
- 860 Renne, P. R., Mundil, R., Balco, G., Min, K., & Ludwig, K. R. (2010). Joint determination of 40K decay constants
861 and $^{40}\text{Ar}^*/^{40}\text{K}$ for the Fish Canyon sanidine standard, and improved accuracy for $^{40}\text{Ar}/^{39}\text{Ar}$ geochronology.
862 *Geochimica et Cosmochimica Acta*, 74(18), 5349–5367. <https://doi.org/10.1016/J.GCA.2010.06.017>
- 863 Rioux, M., Bowring, S., Kelemen, P., Gordon, S., Miller, R., & Dudás, F. (2013). Tectonic development of the
864 Samail ophiolite: High-precision U–Pb zircon geochronology and Sm–Nd isotopic constraints on crustal
865 growth and emplacement. *Journal of Geophysical Research: Solid Earth*, 118(5), 2085–2101.
866 <https://doi.org/10.1002/jgrb.50139>
- 867 Rioux, M., Garber, J., Bauer, A., Bowring, S., Searle, M., Kelemen, P., & Hacker, B. (2016). Synchronous
868 formation of the metamorphic sole and igneous crust of the Semail ophiolite: New constraints on the tectonic
869 evolution during ophiolite formation from high-precision U–Pb zircon geochronology. *Earth and Planetary*
870 *Science Letters*, 451, 185–195. <https://doi.org/10.1016/j.epsl.2016.06.051>
- 871 Roy, D. K., Acharyya, S. K., Ray, K. K., Lahiri, T. C., & Sen, M. K. (1988). Nature of occurrence and depositional
872 environment of the oceanic pelagic sediments associated with the ophiolite assemblage, South Andaman
873 Island. *Indian Minerals*, 42, 31–56.
- 874 Saha, A., Dhang, A., Ray, J., Chakraborty, S., & Moecher, D. (2010). Complete preservation of ophiolite suite from
875 south Andaman, India: A mineral-chemical perspective. *Journal of Earth System Science*, 119(3), 365–381.
876 <https://doi.org/10.1007/s12040-010-0017-6>
- 877 Sarma, D. S., Jafri, S. H., Fletcher, I. R., & McNaughton, N. J. (2010). Constraints on the Tectonic Setting of the
878 Andaman Ophiolites, Bay of Bengal, India, from SHRIMP U–Pb Zircon Geochronology of Plagiogranite. *The*
879 *Journal of Geology*, 118(6), 691–697. <https://doi.org/10.1086/656354>
- 880 Sengupta, S., Ray, K. K., & Acharyya, S. K. (1990). Nature of ophiolite occurrences along the eastern margin of the
881 Indian plate and Nature of ophiolite occurrences along the eastern margin of the Indian plate and their tectonic
882 significance. [https://doi.org/10.1130/0091-7613\(1990\)018<0439](https://doi.org/10.1130/0091-7613(1990)018<0439)
- 883 Shapiro, M. N., & Solov'ev, A. V. (2009). Formation of the Olyutorsky–Kamchatka foldbelt: a kinematic model.
884 *Russian Geology and Geophysics*, 50(8), 668–681. <https://doi.org/10.1016/J.RGG.2008.10.006>
- 885 Singh, A. K., Chung, S.-L., Bikramaditya, R. K., & Lee, H. Y. (2017). New U–Pb zircon ages of plagiogranites from
886 the Nagaland–Manipur Ophiolites, Indo-Myanmar Orogenic Belt, NE India. *Journal of the Geological*
887 *Society*, 174(1), 170–179. <https://doi.org/10.1144/jgs2016-048>
- 888 Singh, S. C., Moeremans, R., McArdle, J., & Johansen, K. (2013). Seismic images of the sliver strike-slip fault and
889 back thrust in the Andaman–Nicobar region. *Journal of Geophysical Research: Solid Earth*, 118(10), 5208–
890 5224. <https://doi.org/10.1002/jgrb.50378>
- 891 Solomon, M. (1990). Subduction, arc reversal, and the origin of porphyry copper–gold deposits in island arcs.
892 *Geology*, 18(7), 630–633. [https://doi.org/10.1130/0091-7613\(1990\)018<0630:SARATO>2.3.CO;2](https://doi.org/10.1130/0091-7613(1990)018<0630:SARATO>2.3.CO;2)
- 893 Soret, M., Agard, P., Dubacq, B., Vitale-Brovarone, A., Monié, P., Chauvet, A., et al. (2016). Strain localization and
894 fluid infiltration in the mantle wedge during subduction initiation: Evidence from the base of the New
895 Caledonia ophiolite. *Lithos*, 244, 1–19. <https://doi.org/10.1016/j.lithos.2015.11.022>
- 896 Soret, M., Agard, P., Dubacq, B., Plunder, A., & Yamato, P. (2017). Petrological evidence for stepwise accretion of
897 metamorphic soles during subduction infancy (Semail ophiolite, Oman and UAE). *Journal of Metamorphic*
898 *Geology*, 35(9), 1051–1080. <https://doi.org/10.1111/jmg.12267>
- 899 Stern, R. J. (2004). Subduction initiation: spontaneous and induced. *Earth and Planetary Science Letters*, 226(3–4),
900 275–292. <https://doi.org/10.1016/j.epsl.2004.08.007>
- 901 Stern, R. J., & Gerya, T. (2017). Subduction initiation in nature and models: A review. *Tectonophysics*, (October).
902 <https://doi.org/10.1016/j.tecto.2017.10.014>
- 903 Stern, R. J., Reagan, M. K., Ishizuka, O., Ohara, Y., & Whattam, S. A. (2012). To understand subduction initiation,
904 study forearc crust: To understand forearc crust, study ophiolites. *Lithosphere*, 4(May), 469–483.
905 <https://doi.org/10.1130/L183.1>
- 906 Syracuse, E. M., & Abers, G. A. (2006). Global compilation of variations in slab depth beneath arc volcanoes and
907 implications. *Geochemistry, Geophysics, Geosystems*, 7(5), n/a–n/a. <https://doi.org/10.1029/2005GC001045>

- 908 Tate, G. W., McQuarrie, N., van Hinsbergen, D. J. J., Bakker, R. R., Harris, R., & Jiang, H. (2015). Australia going
909 down under: Quantifying continental subduction during arc-continent accretion in Timor-Leste. *Geosphere*,
910 *11*(6), 1860–1883. <https://doi.org/10.1130/GES01144.1>
- 911 Vaes, B., van Hinsbergen, D. J. J., & Boschman, L. M. (2019). Reconstruction of Subduction and Back-Arc
912 Spreading in the NW Pacific and Aleutian Basin: Clues to Causes of Cretaceous and Eocene Plate
913 Reorganizations. *Tectonics*, *0*(0). <https://doi.org/10.1029/2018TC005164>
- 914 Wakabayashi, J., & Dilek, Y. (2000). Spatial and temporal relationships between ophiolites and their metamorphic
915 soles: A test of models of forearc ophiolite genesis. *Geological Society of America Special Papers*,
916 *349*(January), 53–64. <https://doi.org/10.1130/0-8137-2349-3.53>
- 917 Wakabayashi, J., & Dilek, Y. (2003). What constitute “emplacement” of an ophiolite?: Mechanisms and relationship
918 to subduction initiation and formation of metamorphic soles. *Geological Society, London, Special*
919 *Publications*, *218*, 427–447.
- 920 Wang, J. G., Wu, F. Y., Tan, X. C., & Liu, C. Z. (2014). Magmatic evolution of the Western Myanmar Arc
921 documented by U-Pb and Hf isotopes in detrital zircon. *Tectonophysics*, *612–613*, 97–105.
922 <https://doi.org/10.1016/j.tecto.2013.11.039>
- 923 White, R. W., Powell, R., & Clarke, G. L. (2002). The interpretation of reaction textures in Fe-rich metapelitic
924 granulites of the Musgrave Block, Central Australia: Constraints from mineral equilibria calculations in the
925 system. *Journal of Metamorphic Geology*, *20*(1), 41–55. <https://doi.org/10.1046/j.0263-4929.2001.00349.x>
- 926 White, R. W., Powell, R., Holland, T. J. B., Johnson, T. E., & Green, E. C. R. (2014). New mineral activity-
927 composition relations for thermodynamic calculations in metapelitic systems. *Journal of Metamorphic*
928 *Geology*, *32*(3), 261–286. <https://doi.org/10.1111/jmg.12071>
- 929 Whitney, D. L., & Evans, B. W. (2010). Abbreviations for names of rock-forming minerals. *American Mineralogist*,
930 *95*(1), 185–187. <https://doi.org/10.2138/am.2010.3371>
- 931 Woodcock, N. H., & Robertson, A. H. F. (1977). Origins of some ophiolite-related metamorphic rocks of the
932 “Tethyan” belt. *Geology*, *5*, 373–376. [https://doi.org/10.1130/0091-7613\(1977\)5<373](https://doi.org/10.1130/0091-7613(1977)5<373)
- 933 Zhang, X., Chung, S.-L., Lai, Y.-M., Ghani, A. A., Murtadha, S., Lee, H.-Y., & Hsu, C.-C. (2019). A 6000-km-long
934 Neo-Tethyan arc system with coherent magmatic flare-ups and lulls in South Asia. *Geology*, *47*(6), 573–576.
935 <https://doi.org/10.1130/g46172.1>
- 936 Zhou, X., Li, Z. H., Gerya, T. V., Stern, R. J., Xu, Z., & Zhang, J. (2018). Subduction initiation dynamics along a
937 transform fault control trench curvature and ophiolite ages. *Geology*, *46*(7), 607–610.
938 <https://doi.org/10.1130/G40154.1>
- 939
- 940
- 941
- 942
- 943
- 944
- 945
- 946
- 947
- 948

949 **Figure caption**

950

951 *Figure 1: Conceptual sketch of subduction polarity reversal. The first stage depict oceanic subduction*
 952 *below a mature arc. The red lines shows the subduction interface where one lithosphere slide against the*
 953 *other one. The second sketch depicts the continent entering the subduction zone and the red star emphasis*
 954 *the collision between the continent and the arc. The dashed red line shows the mechanically weak place*
 955 *where the new subduction will start. The third cartoons shows the effective subduction polarity reversal.*
 956 *The red lines again shows the subduction interface where one lithosphere slide against the other one. The*
 957 *cartoon is inspired by Chemenda et al. (2001).*

958

959 *Figure 2: (a) Location of the Andaman Island in the Indian Ocean realm (modified from Ghosh et al.*
 960 *(2017)). (b) Schematic geological map of the Andaman Islands modified from Ghosh et al. (2017). (c)*
 961 *Sketch of the investigated area redrawn from field observation. Color of the symbols denotes the nature of*
 962 *the rock. The shape of the symbol denotes the character of the observation / sample: in situ of flying*
 963 *blocks. (d) Field view of the in situ clinopyroxene bearing amphibolite (AN1709a sample). The red star*
 964 *refers to the position of sample AN1709 on the localization map. Both inset show more detailed picture*
 965 *on the in-situ location and of a boulder (sample AN1704). The right panel shows the in-situ location of*
 966 *the greenschist facies metamorphic sole characterized by the alternation of mafic and quartz-rich layers.*
 967 *The pink star refers to the position on the map. Mineral abbreviations are after Whitney & Evans (2010)*

968

969 *Figure 3: microphotographs of representative sole samples. All mineral abbreviations are after Whitney*
 970 *& Evans, (2010). (a) Plain polarised light (PPL) view of a quartz rich sample. Late fracture are filled*
 971 *with adularia. (b) PPL picture showing the initial clinopyroxene still preserved in sample AN1704a. (c)*
 972 *PPL vie of the matrix made of amphibole and plagioclase. (d) Close up on a clinopyroxene with*
 973 *amphibole inclusions. (e) Close up on an amphibole with inclusion of rutile and. (f) Inclusion of rutile in*
 974 *titanite at the edge of an amphibole. (g) Rutile inclusion in titanite. (h) Cross polarised picture of late*
 975 *fillings of adularia with overgrowing actinolite on high temperature amphibole. (i) General PPL view of*
 976 *sample AN1709a depicting the main foliation and rutile and ilmenite coexisting with amphibole and*
 977 *plagioclase. (j,k) PPL and XPL view of the preserved clinopyroxene in sample AN1709a. Note the big*
 978 *rutile included in titanite (l) Backscattered picture of sample AN1709d showing the general texture.*
 979 *Arrows indicate titanite rim over rutile. (m) Close up view of a plagioclase with needles of epidote*
 980 *growing in places. (n,o) PPL and XPL views of sample AN1709e showing clinopyroxene and green*
 981 *amphibole overgrowth.*

982

983 *Figure 4: Chemical composition of minerals from the metamorphic sole. (a) Amphibole: Ti a.p.f.u vs. Si*
 984 *a.p.f.u. (b) Amphibole: Mg# vs. Si a.p.f.u. with $Mg\# = Mg/(Mg+Fe^{2+})$ (c) Ternary representation of the*
 985 *feldspar. Analysis close to the K feldspar pole correspond to adularia in late vein. (d) Ternary*
 986 *representation of clinopyroxene. Mineral abbreviations are after Whitney & Evans (2010).*

987 *Figure 5: Degassing spectra for samples a) AN1704a and b) AN1709a. Steps 16 and 17 are omitted in the*
 988 *age calculation. The terms MSWD, P and WMPA denote mean squared weighted deviance, probability of*
 989 *fit and weighted mean plateau age, respectively. The K/Ca ration is calculated as $^{39}Ar/^{37}Ar$.*

990 *Figure 6: (a) Results of the hornblende-plagioclase empirical thermobarometry. (b) Temperature vs.*
 991 *XH_2O pseudosection with $XFe^{3+} = 0.12$. PT pseudosection for different amounts of water. (c)*
 992 *Temperature vs. XH_2O pseudosection with $XFe^{3+} = 0.19$. PT pseudosection for different amounts of*
 993 *water. (d) Temperature vs. XH_2O pseudosection with $XFe^{3+} = 0.25$. PT pseudosection for different*
 994 *amounts of water.*

995

996 *Figure 7: Tentative geodynamic reconstruction of the Andaman ophiolite. (a) ca. 126 Ma: initiation of a*
 997 *new subduction zone upon collision of the northern extension of the Woyla arc. The Ngalau plate is*
 998 *consuming on both side (Advokaat et al., 2018), and arc magmatism exists on both Sundaland and in the*
 999 *Woyla arc. (b) ca 116 Ma: the new subduction zone propagates southwards. Arc magmatism on*
 1000 *Sundaland cease in the northern part (Lin et al., 2019). (c) ca. 106 Ma: The gray star indicates the*
 1001 *moment when the northernmost part of the Woyla arc starts to collide with Sundaland. At that time the*
 1002 *Andaman metamorphic sole is exhuming (our data) and SSZ gabbros are crystallising. (d) ca. 99-95 Ma,*
 1003 *Arc magmatism starts above the new North-Eastwards dipping subduction as attested by the*
 1004 *agglomerates of the Andaman Islands. Most of the Woyla arc is accreted to Sundaland (Advokaat et al.,*
 1005 *2018). The BAB abbreviation shows the approximate location the back arc basin. Dotted red line denotes*
 1006 *the weak place where the new subduction will start. Double lines show the position of the back arc*
 1007 *spreading centre.*

1008

1009 **Table caption**

1010

1011 Table 1: sample list, location and mineral occurrences. Mineral abbreviation are after Whitney &
 1012 Evans, (2010). Other abbreviation are the following: A, amphibolite facies; GS, greenschist
 1013 facies;

1014 Lines in bold correspond to sample for which we present probe data. Sample in grey is the one
 1015 used for PT determination using pseudosection.

1016

1017 Table 2: selection of representative analysis for amphibole, clinopyroxene and feldspar.

1018

1019 Table 3: Ar/Ar data. Abbreviation: n number of steps taken for age calculation.

1020

1021 Table 4: Bulk composition (mol %) for sample AN1709a used for pseudosection modelling. The
 1022 table reports all bulk used for Fig. 6. Abbreviation: LOI, Loss on ignition; SS, Unsaturated sub
 1023 solidus water content; MSWD, mean square of weighted deviates; TGA, total gas age, P
 1024 probability density fit.

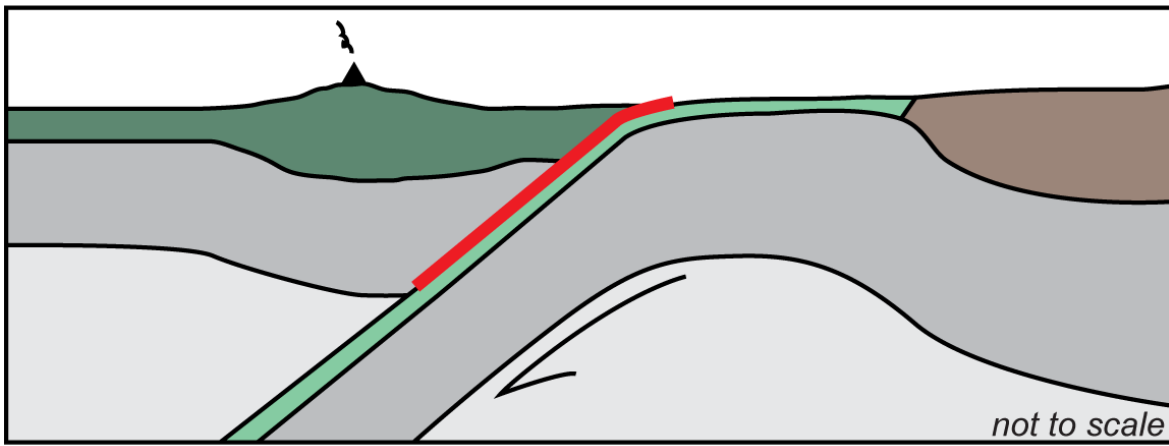
1025

Figure 1.

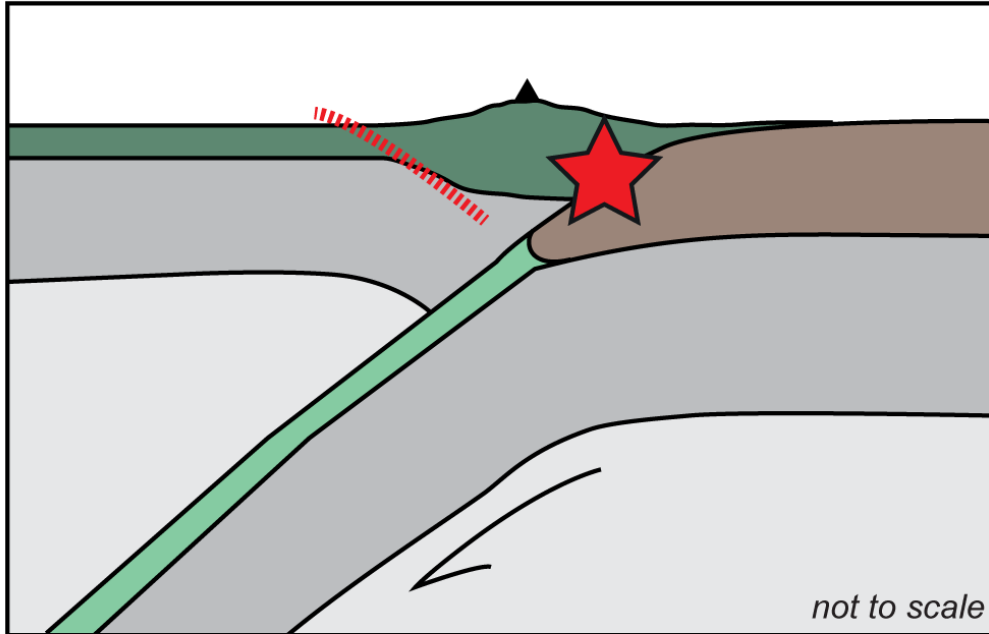
Arc

Ocean

Cont.



Cont. Arc collision



Effective flip polarity reversal

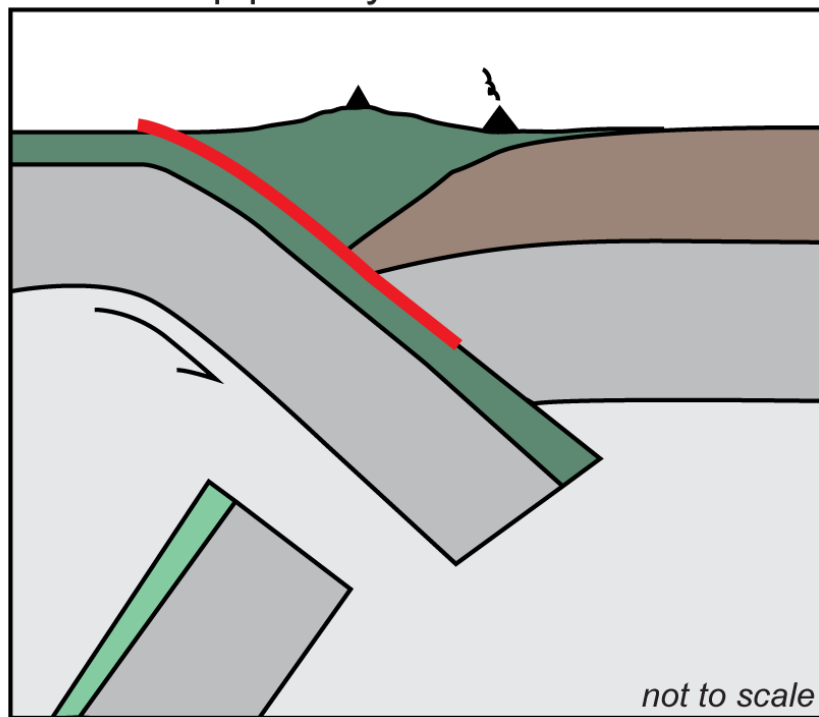


Figure 2.

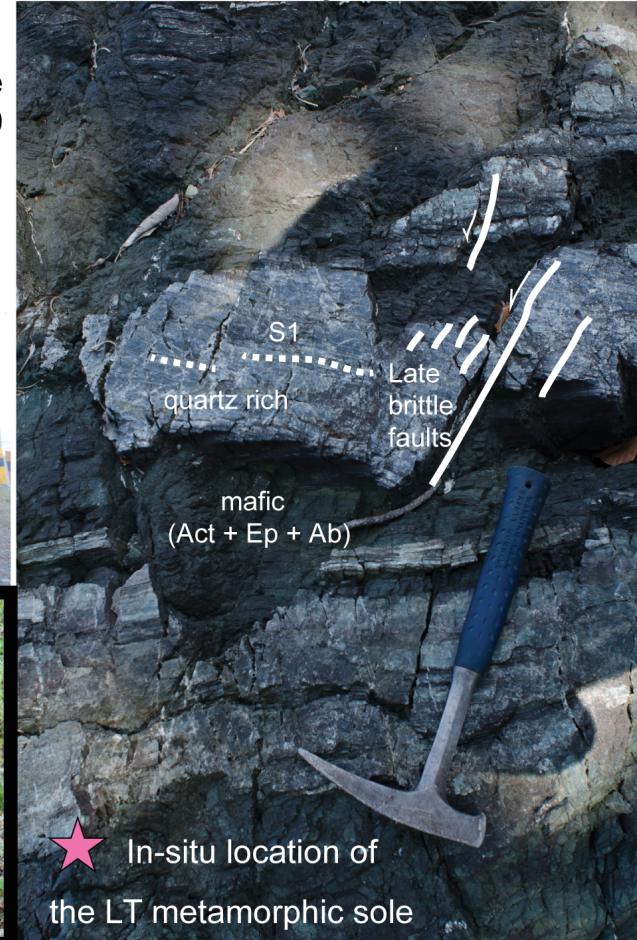
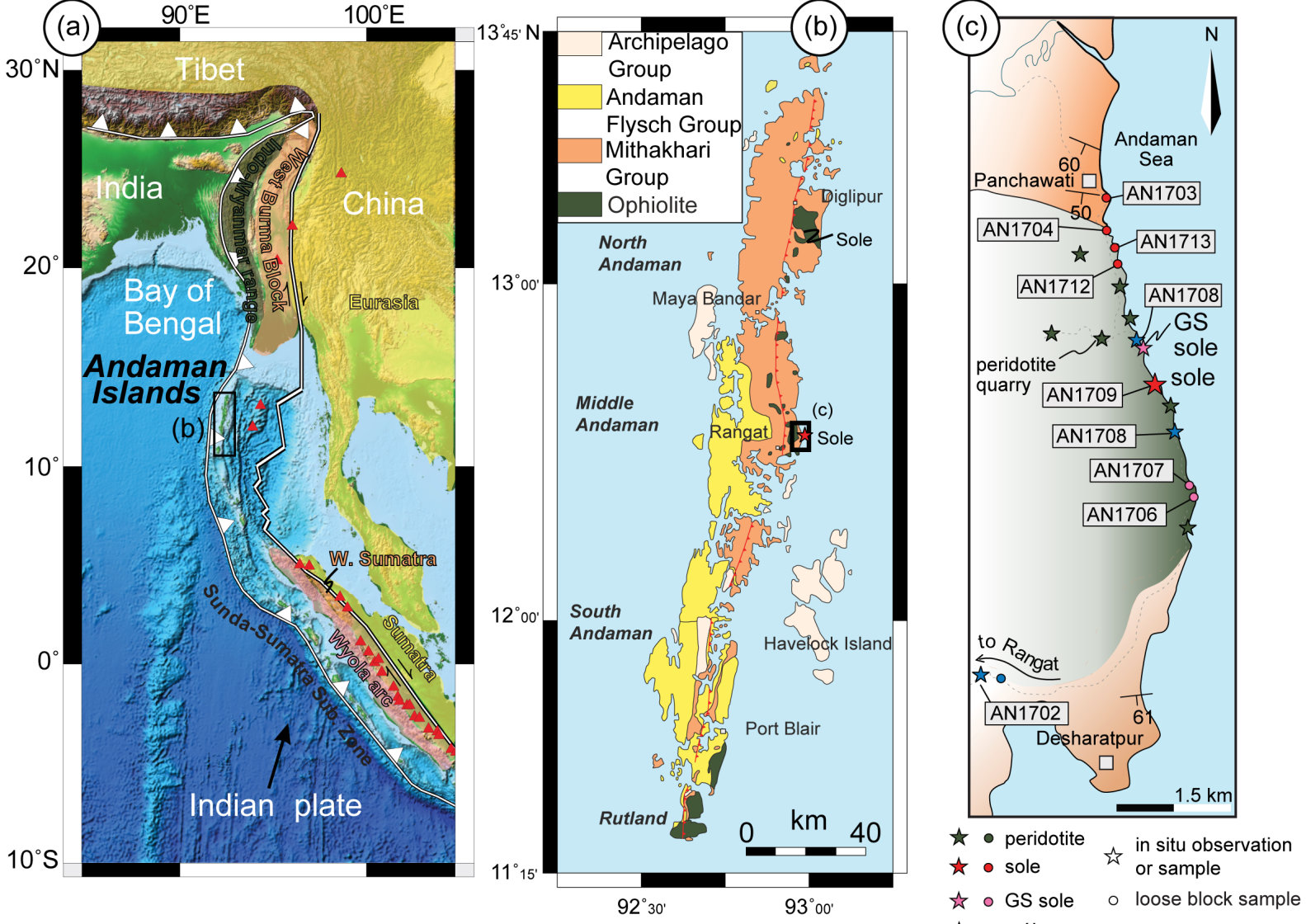


Figure 3.

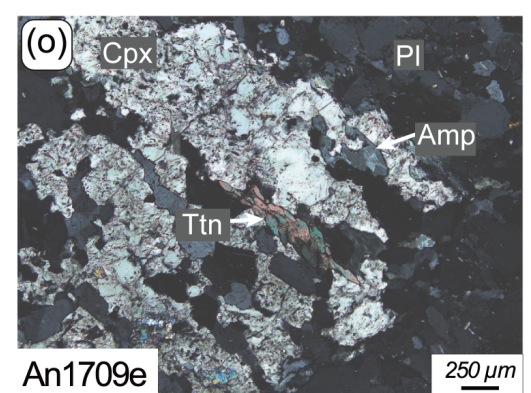
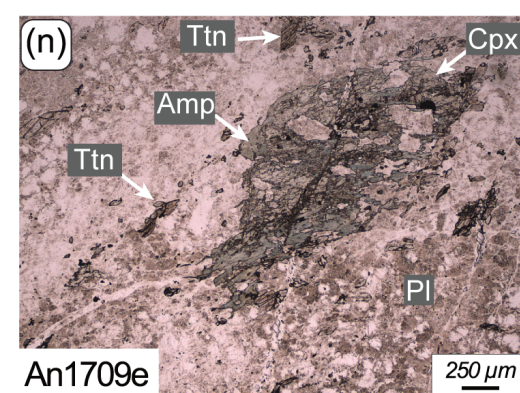
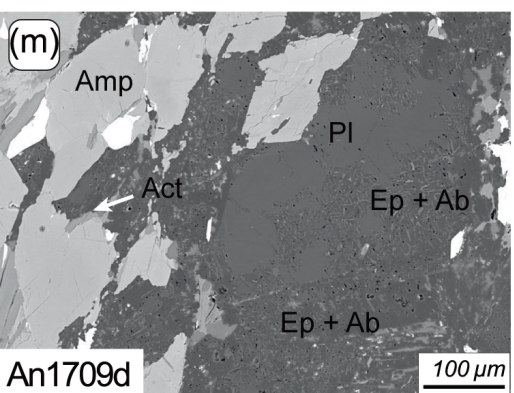
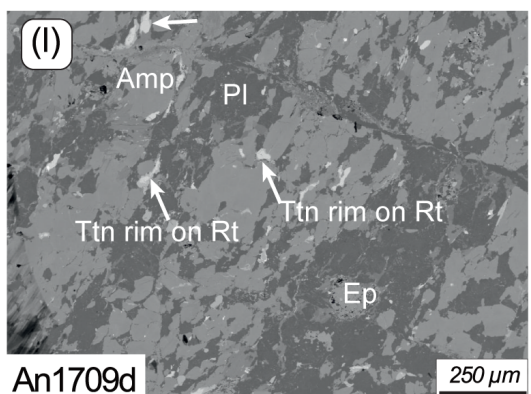
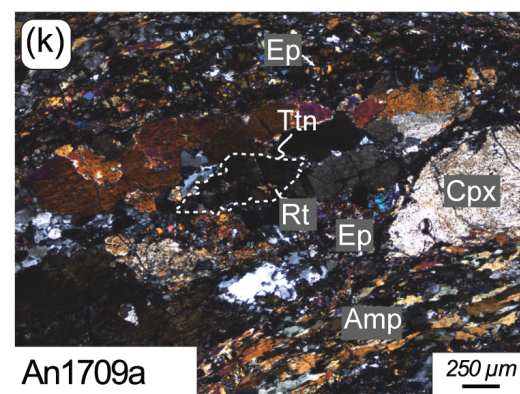
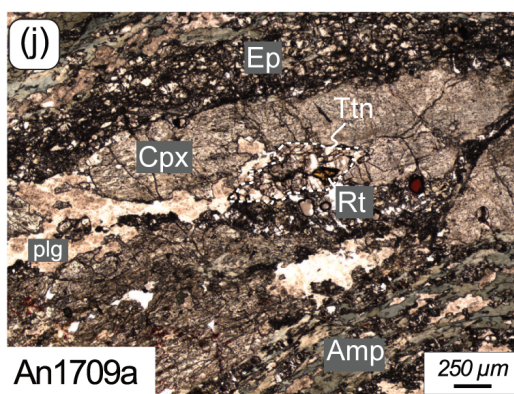
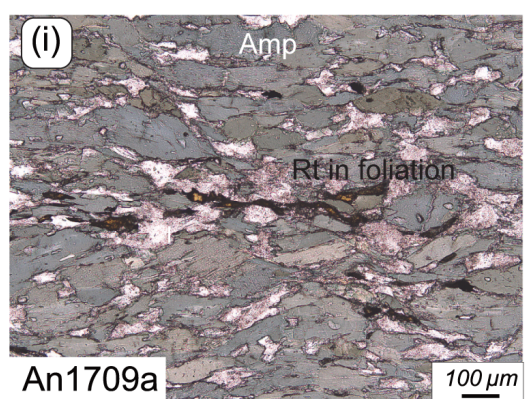
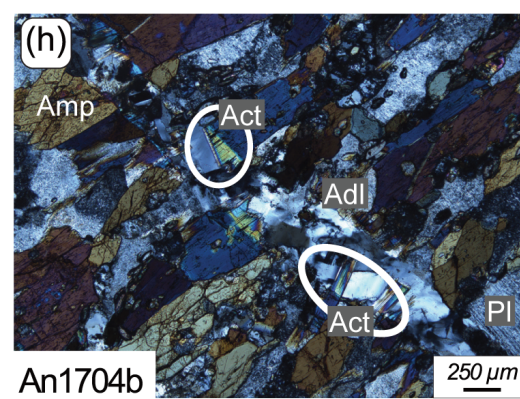
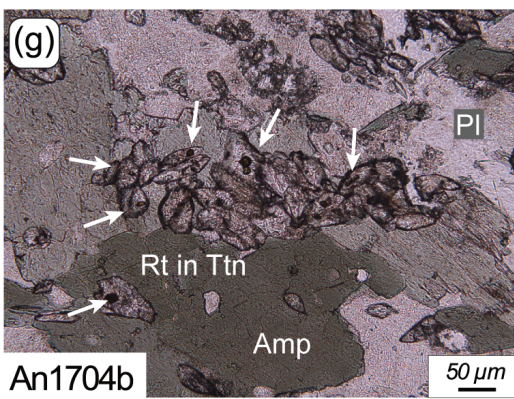
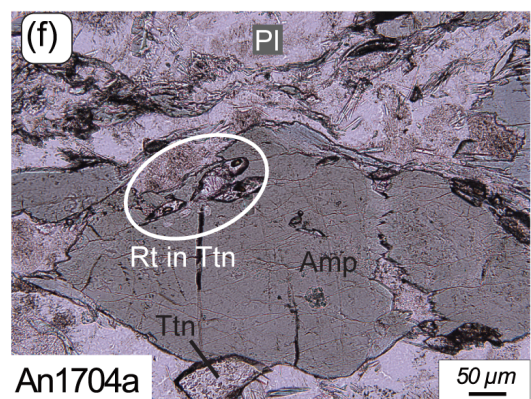
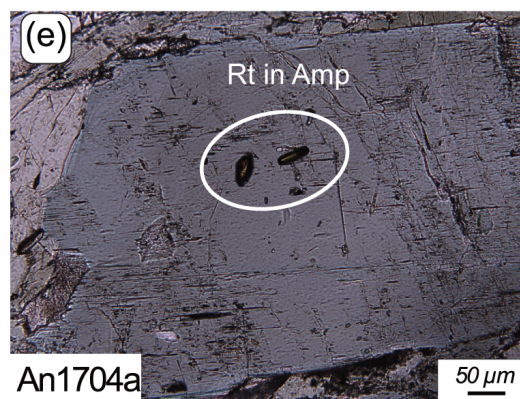
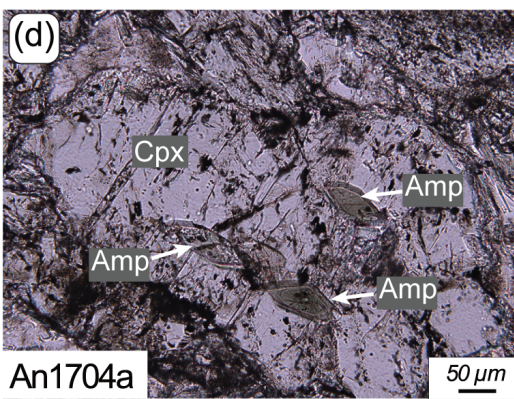
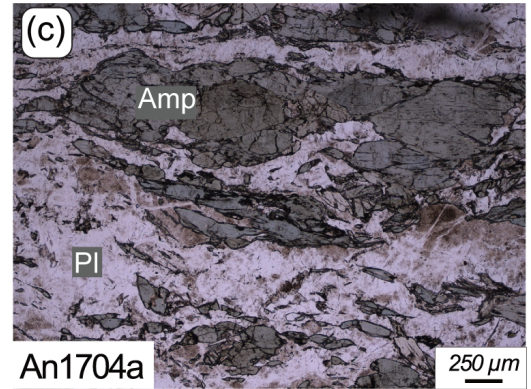
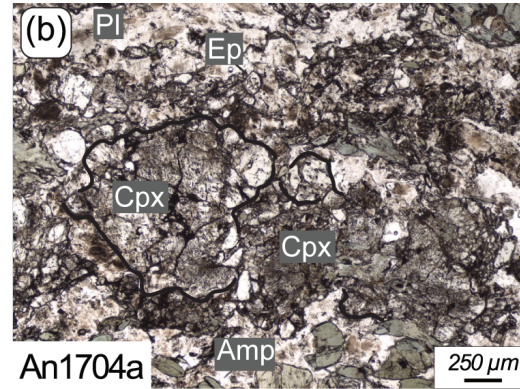
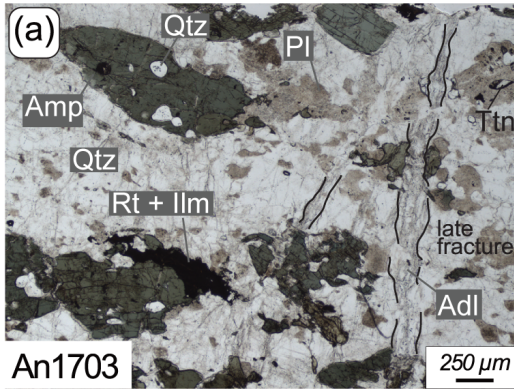


Figure 4.

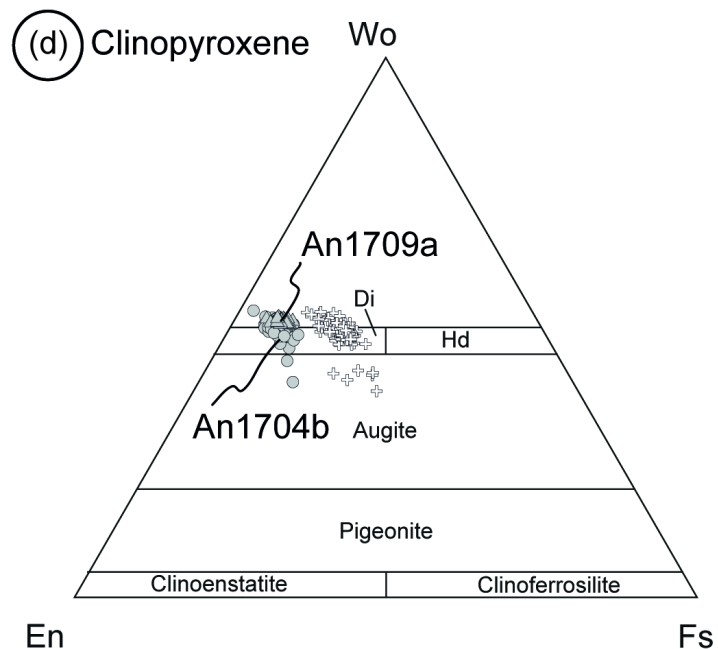
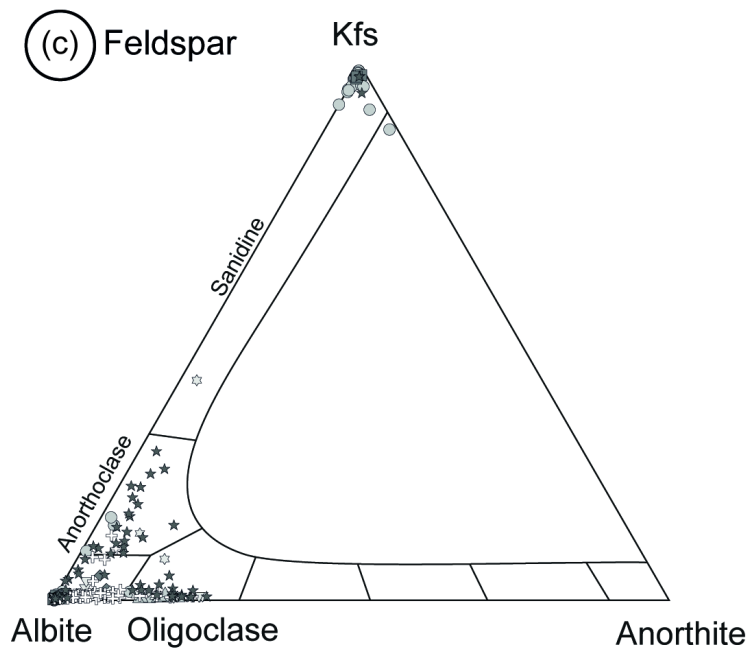
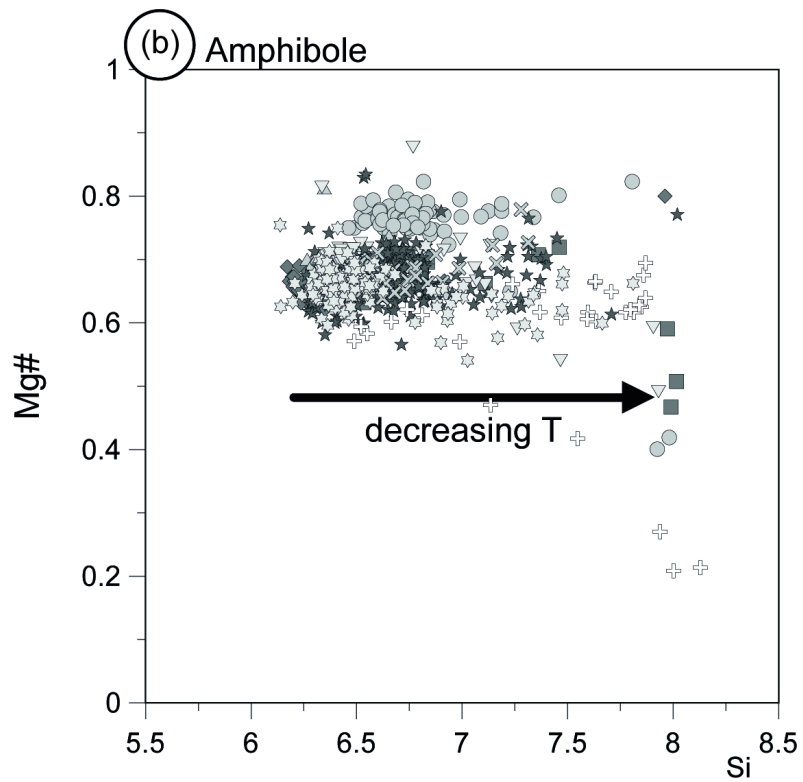
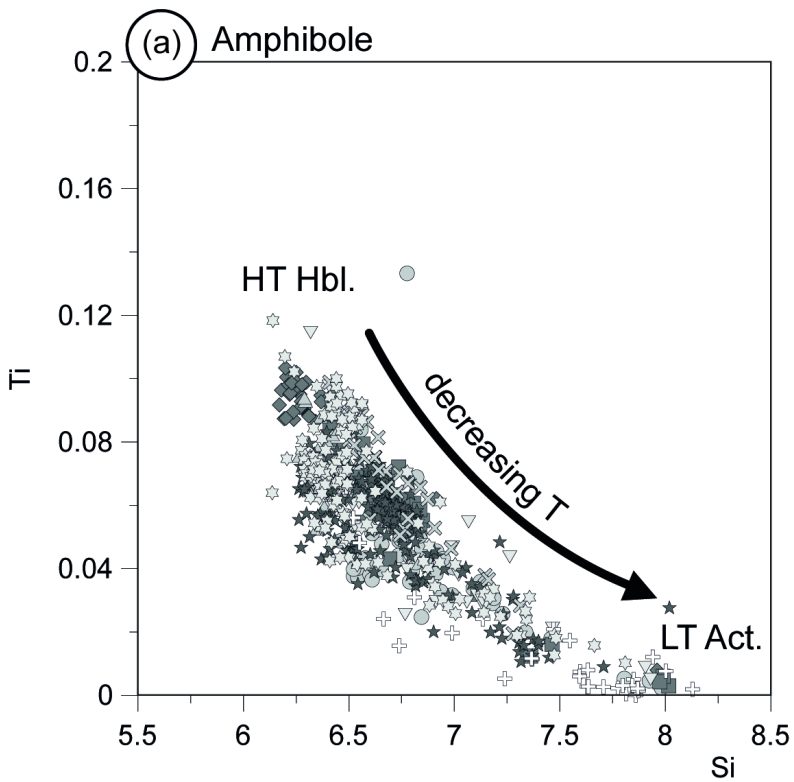
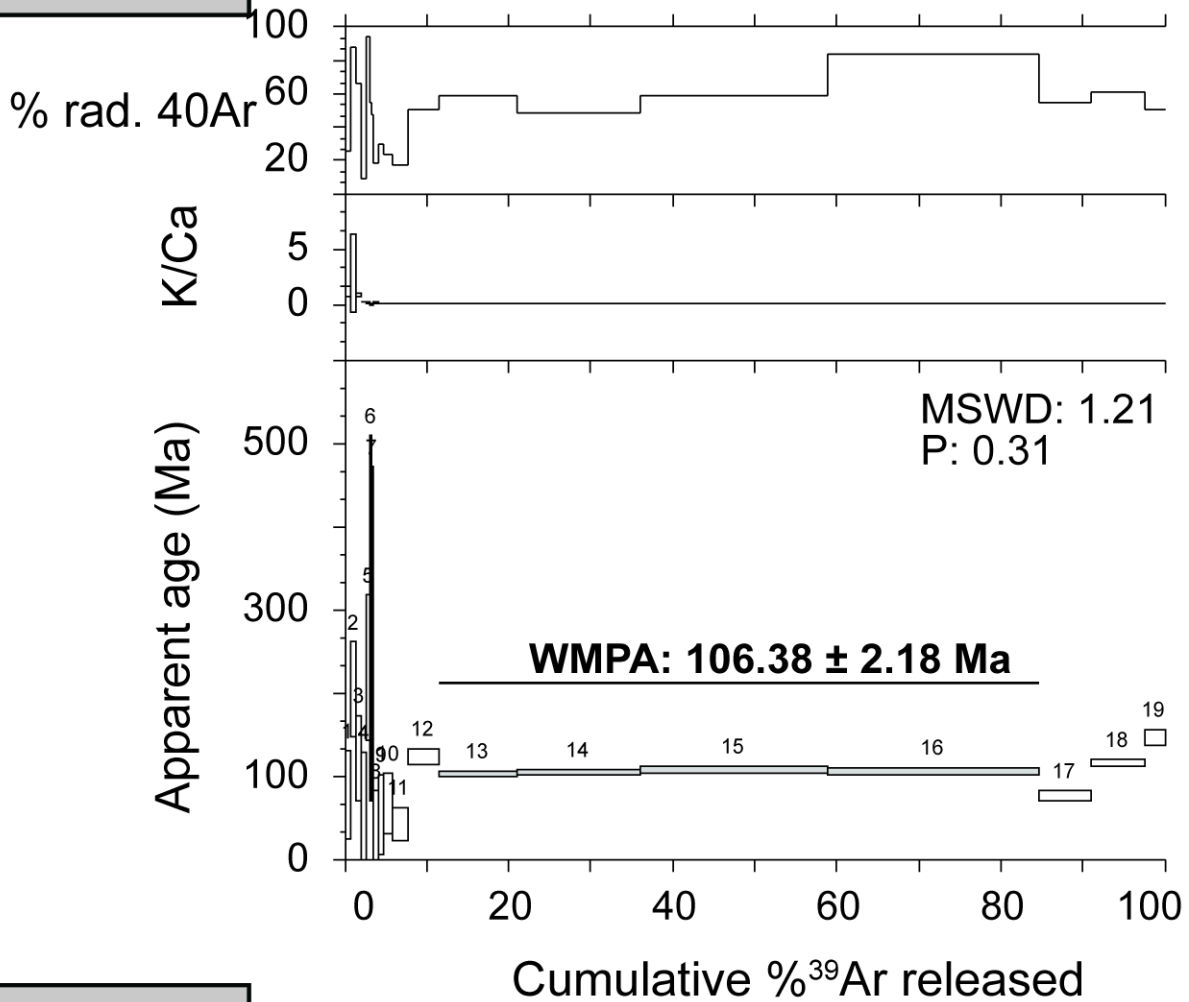


Figure 5.

a. AN1704a



b. AN1709a

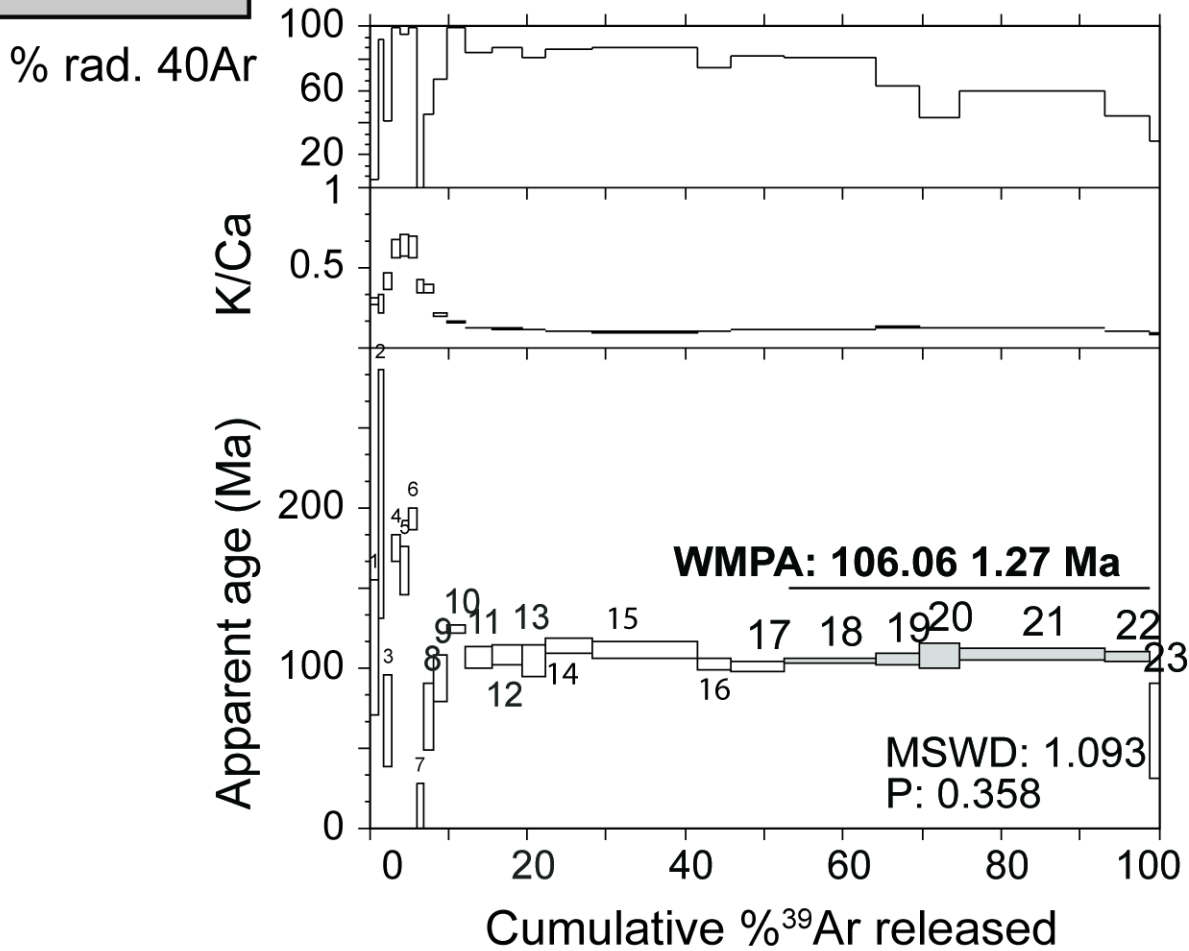


Figure 6.

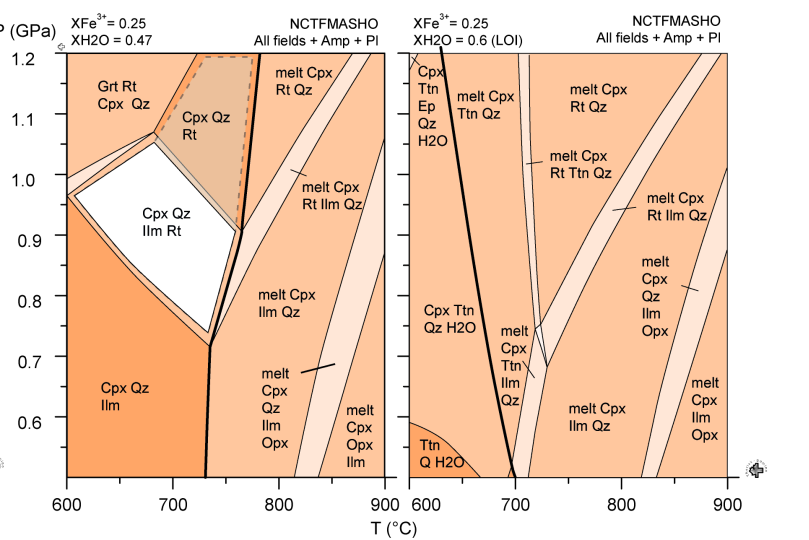
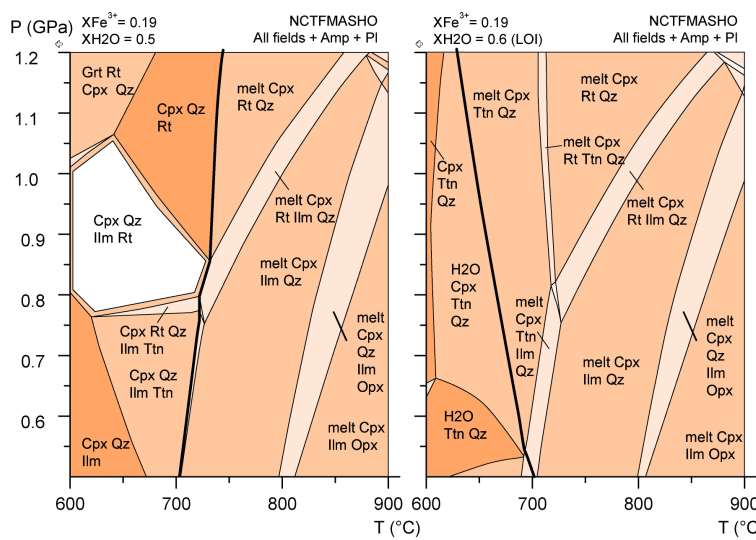
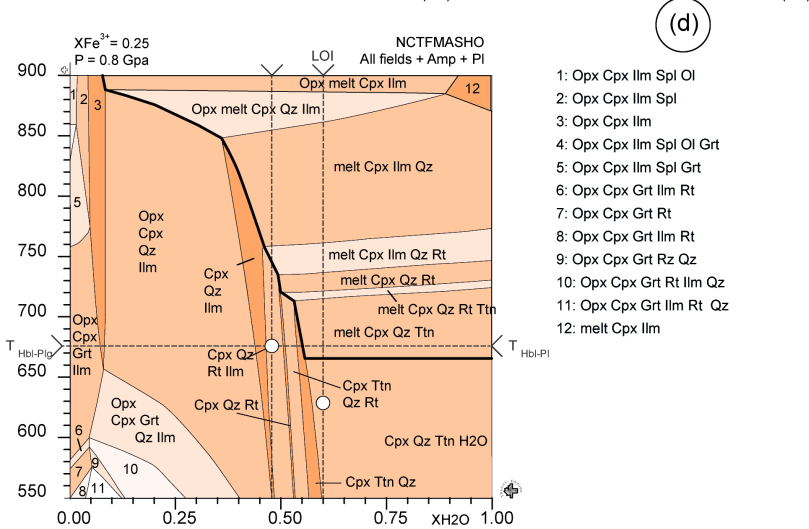
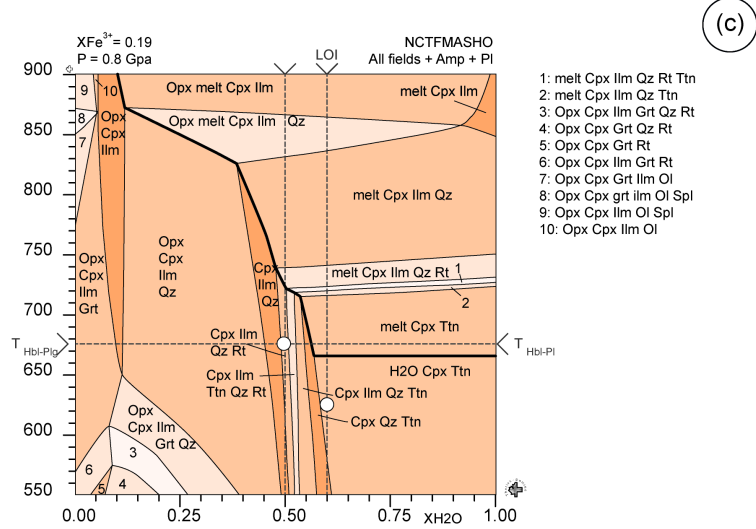
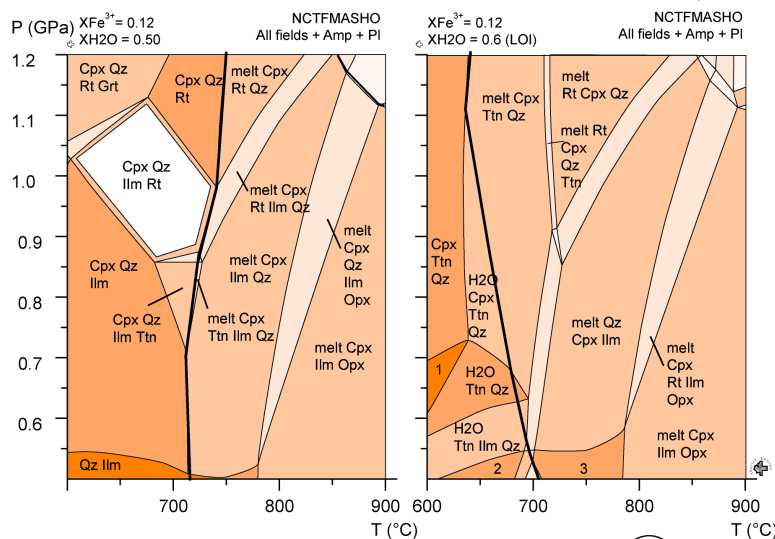
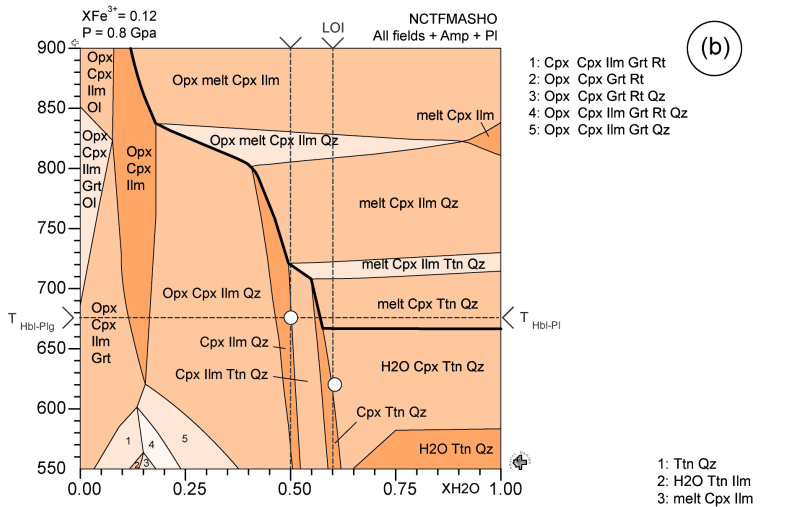
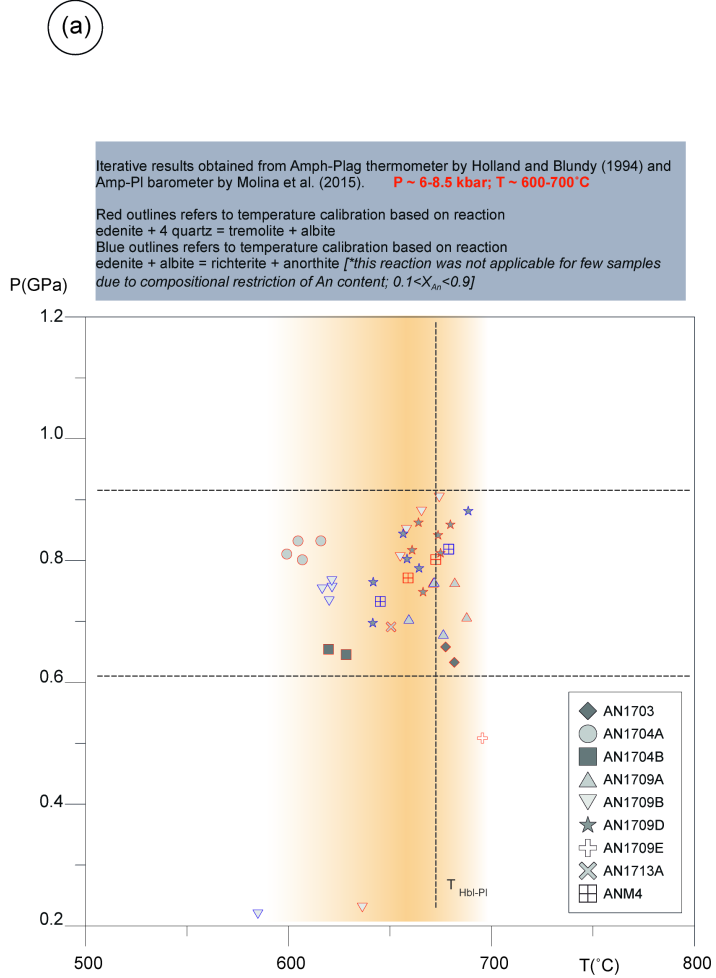


Figure 7.

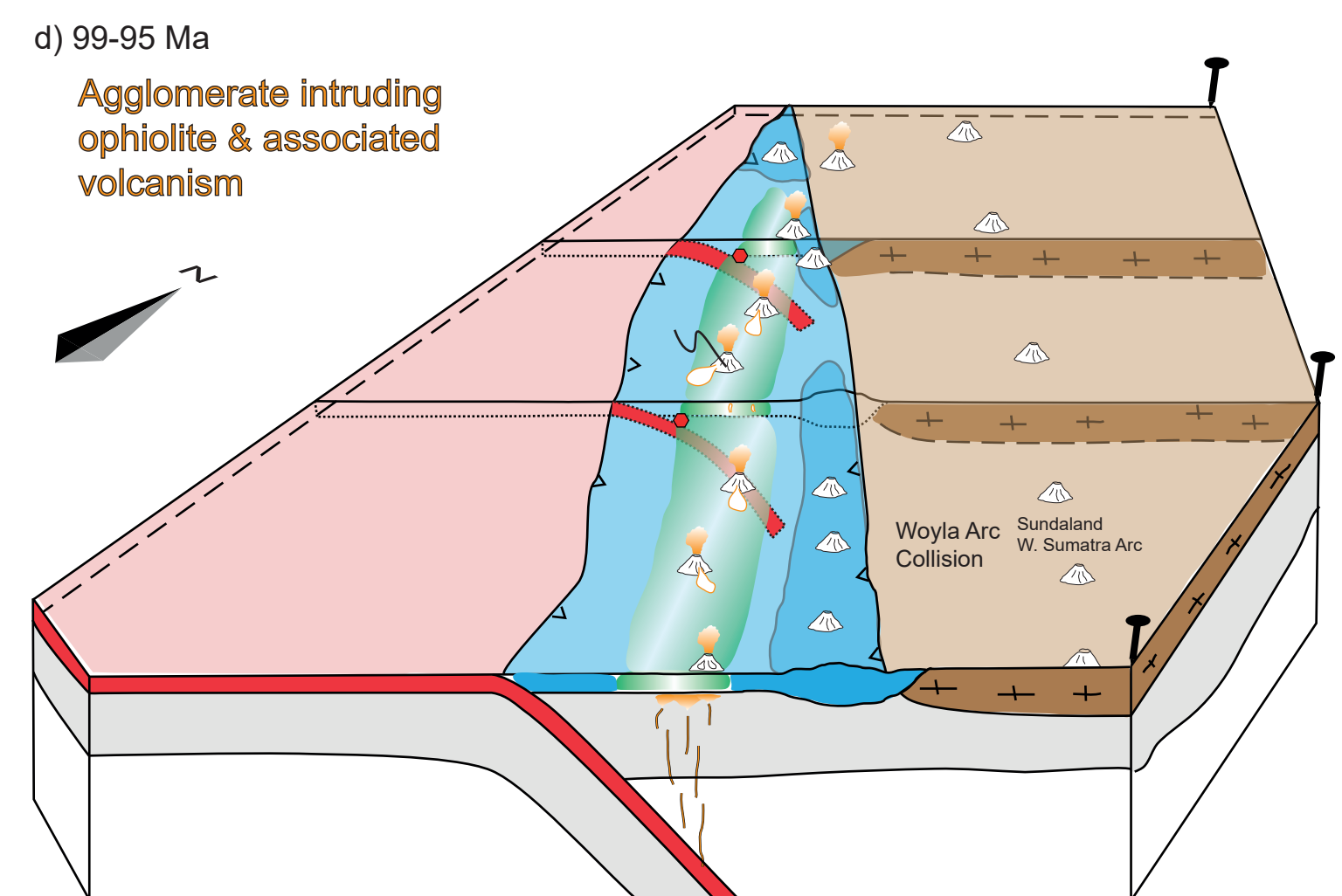
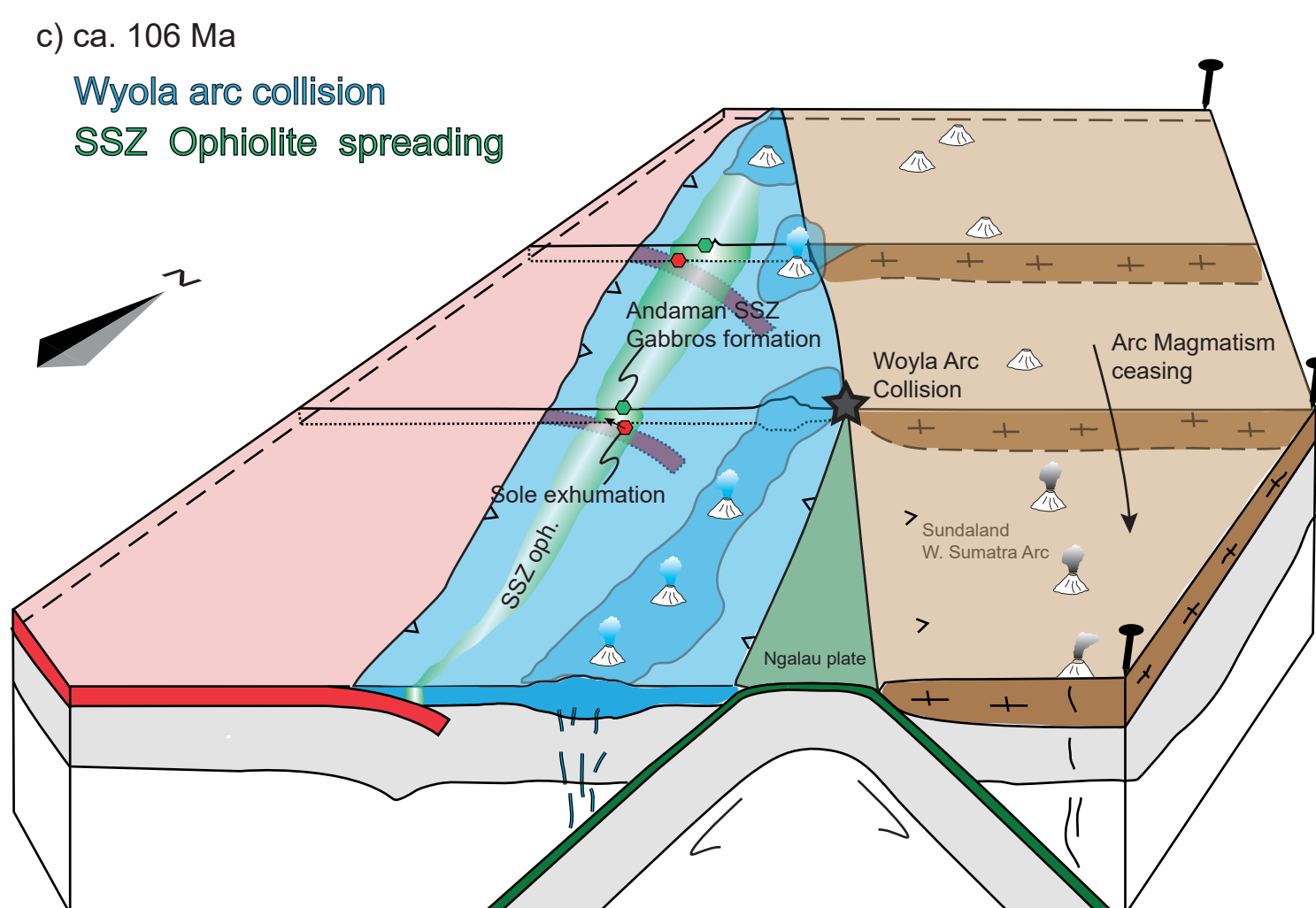
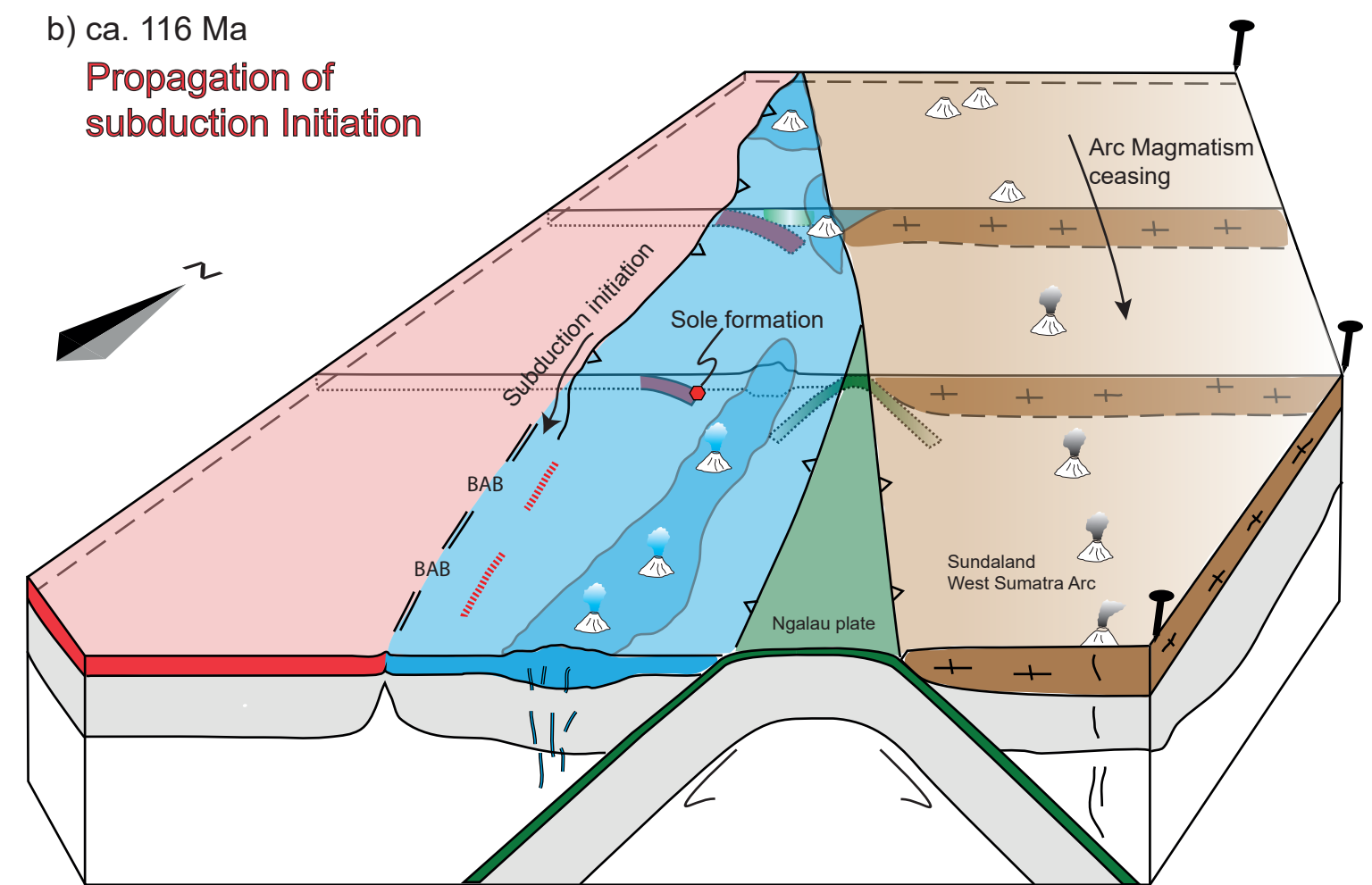
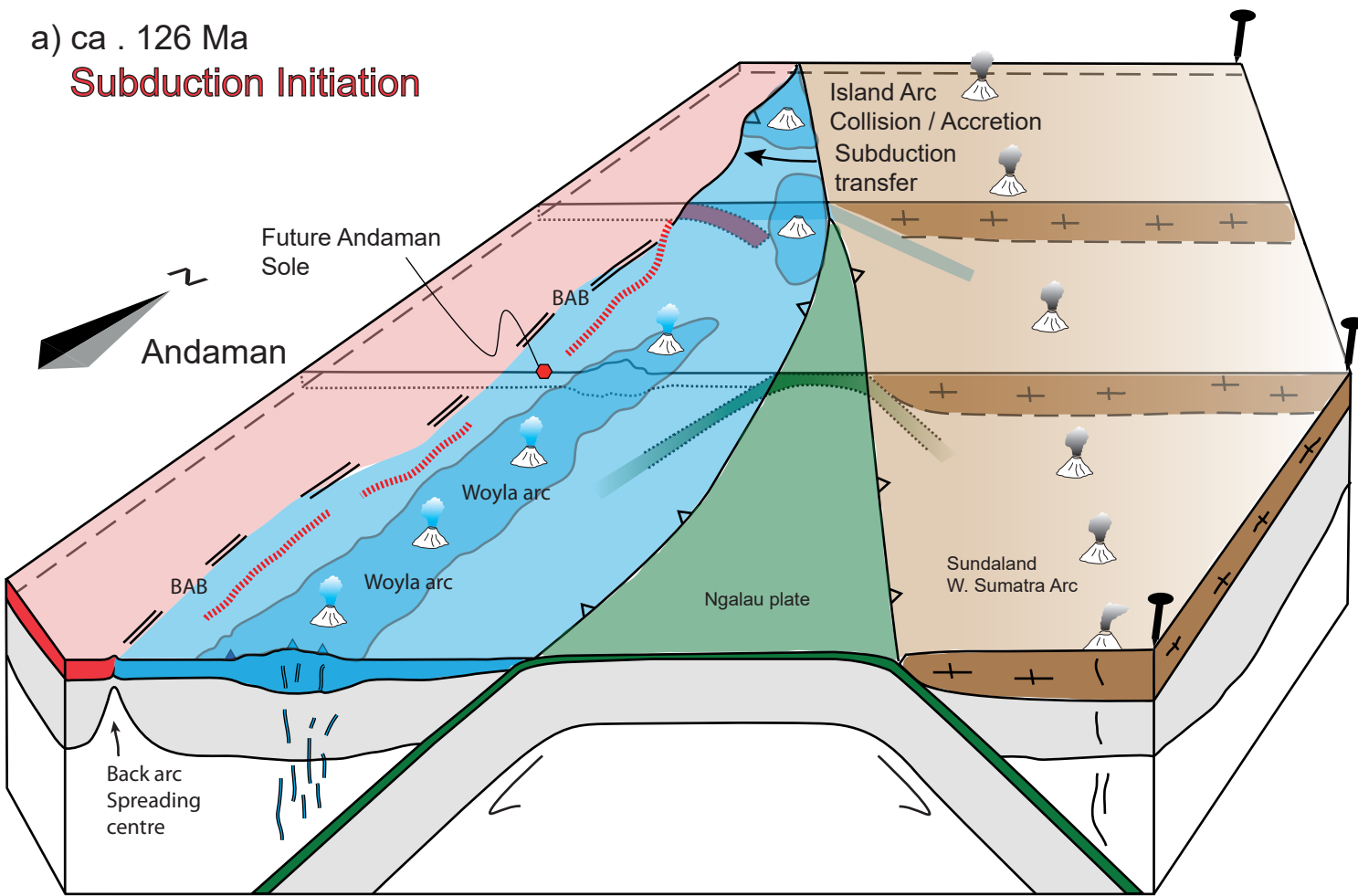


Table 1

Sample code	Location (WGS 84)		Grade	Amph	Plg	Cpx	Ep	Rt	Ttn	Ilm	Ad	Other	Other	Other	
	N (° ' ")	E (° ' ")													
AN1702	12 30 27	092 56 19	Mélange												
AN1703	12 35 44	092 57 27	A	x	x		* (Pl)	x	* (Rt)	* (Rt)	* (v)	* Amp (Amp)	* Mus (Pl)	Qz	
AN1704a	12 35 27	092 57 28	A	x	x	x	* (Pl)	x	* (Rt)	?	* (v)	* Amp (Amp)			
AN1704b	12 35 27	092 57 28	A	x	x		x / * (Pl)	x	x / * (Rt)		* (v)	* Amp (Amp)	* Mus (Pl)		
AN1706a	12 32 31	092 58 31	GS	x	x		x	x	x / * (Rt)						
AN1706b	12 32 31	092 58 31	GS	x	x		x	x	x / * (Rt)		* (v)				
AN1707a	12 32 38	092 58 30	GS	x	x		x		x		* (v)	* Cc (v)			
AN1707b	12 32 38	092 58 30	GS		x		x				* (v)	* Cc (v)	Chl Opq	Qz	
AN1708	12 33 15	092 58 18	Mélange												
AN1709a	12 33 44	092 58 07	A	x	x	x	* / * (Pl)	x	* (Rt)		* (v)	* Chl			
AN1709b	12 33 44	092 58 07	A	x	x		* (Pl) (v)	x	x		* (v)				
AN1709c	12 33 44	092 58 07	A	x	x			x	* (Rt)	* (Rt)		* Amp (Amp)		Qz	
AN1709d	12 33 44	092 58 07	A	x	x		x	x	* (Rt)			Bt?	* Chl (Bt?)		
AN1709e	12 33 44	092 58 07	A	* (cpx)	x	x	x / * (Pl)		x			* Cc	Opq		
AN1712a	12 35 41	092 57 41	A	x	x						* (v)	* Amp (Amp)			
AN1712b	12 35 41	092 57 41	A	x	x		* (v)				* (v)	* Amp (Amp)			
AN1713a	12 35 16	092 57 34	A	x	x			x	x / * (Rt)		* (v)		* Mus (Pl)		
AN1713b	12 35 16	092 57 34	A	x	x		x	x	x / * (Rt)		* (v)	* Amp (Amp)	* Mus (Pl)		
AN1713c	12 35 16	092 57 34	A	x	x		* (Pl)	* (ilm)	* (ilm)	x			* Mus (Pl)		

x main assemblage

* late phase

v veins

Table 2
Amphibole

Sample	AN1703	AN1703	AN1704A	AN1704A	AN1704A	AN1704A	AN1704B	AN1704B	AN1704B	AN1709A
Anal. #	7	12	18	19	2	3	4	7	8	14
SiO2	42.49	42.11	47.19	48.52	52.74	52.41	53.46	45.20	43.42	42.97
TiO2	0.82	0.87	0.47	0.39	0.02	0.04	0.03	0.58	0.69	0.79
Al2O3	12.94	13.18	10.39	9.54	0.16	0.07	0.14	10.25	11.92	12.31
Cr2O3	0.03	0.04	0.12	0.10	0.05	0.00	0.00	0.00	0.02	0.04
FeO	16.62	17.02	11.61	12.01	22.54	23.90	19.08	14.51	14.82	14.69
MnO	0.68	0.68	0.34	0.37	0.48	0.82	0.59	0.43	0.42	0.23
MgO	10.23	10.10	14.07	14.32	9.12	8.57	11.02	11.99	11.17	11.49
CaO	11.10	10.99	12.42	12.56	12.19	12.19	12.18	11.82	11.61	11.14
Na2O	1.91	1.97	1.18	1.01	0.21	0.13	0.20	1.38	1.61	2.05
K2O	0.63	0.67	0.62	0.52	0.03	0.06	0.06	0.53	0.60	0.60
Total	97.45	97.63	98.41	99.34	97.55	98.20	96.75	96.68	96.29	96.30
Formula Unit										
O#	23	23	23	23	23	23	23	23	23	23
Si	6.27	6.21	6.75	6.87	7.98	7.92	8.02	6.67	6.46	6.37
Al iv	1.73	1.79	1.25	1.13	0.02	0.01	0.00	1.33	1.54	1.63
Al vi	0.52	0.50	0.50	0.46	0.01	0.00	0.02	0.45	0.55	0.52
Ti	0.09	0.10	0.05	0.04	0.00	0.00	0.00	0.06	0.08	0.09
Cr	0.00	0.00	0.01	0.01	0.01	0.00	0.00	0.00	0.00	0.00
Fe3+	0.85	0.94	0.38	0.40	0.00	0.13	0.00	0.52	0.56	0.69
Fe2+	1.20	1.16	1.01	1.03	2.85	2.89	2.39	1.28	1.28	1.13
Mn	0.09	0.08	0.04	0.04	0.06	0.11	0.08	0.05	0.05	0.03
Mg	2.25	2.22	3.00	3.02	2.06	1.93	2.46	2.64	2.48	2.54
Ca	1.75	1.74	1.90	1.91	1.98	1.97	1.96	1.87	1.85	1.77
Na	0.55	0.56	0.33	0.28	0.06	0.04	0.06	0.39	0.47	0.59
K	0.12	0.13	0.11	0.09	0.01	0.01	0.01	0.10	0.11	0.11
OH*	2.00	2.00	2.00	2.00	2.00	2.00	2.00	2.00	2.00	2.00
XMg	0.65	0.66	0.75	0.75	0.42	0.40	0.51	0.67	0.66	0.69
XFe3+	0.62	0.65	0.43	0.46	0.04	0.03	0.00	0.53	0.51	0.57

Table 2 cont.

Amphibole

Sample	AN1709A	AN1709B	AN1709D	AN1709D	AN1709E	AN1709E	AN1709E	AN1713A
Anal. #	3	23	12	57	4	5	6	20
SiO2	42.74	43.95	44.00	52.60	53.23	50.60	46.59	44.82
TiO2	0.64	0.63	0.70	0.08	0.00	0.19	0.17	0.63
Al2O3	12.15	12.15	12.67	2.87	1.62	3.97	6.84	10.43
Cr2O3	0.04	0.01	0.03	0.00	0.01	0.00	0.04	0.08
FeO	14.81	14.03	14.15	15.27	14.68	16.09	18.19	13.41
MnO	0.30	0.25	0.21	0.38	1.72	1.04	1.12	0.25
MgO	11.43	11.52	11.57	13.13	13.20	12.26	10.52	12.20
CaO	11.45	11.30	11.33	12.22	12.77	12.11	11.92	11.46
Na2O	2.18	1.62	1.83	0.42	0.20	0.65	1.12	1.73
K2O	0.58	0.30	0.56	0.28	0.06	0.32	0.52	0.47
Total	96.32	95.76	97.04	97.26	97.49	97.23	97.04	95.48
Formula Unit								
O#	23	23	23	23	23	23	23	23
Si	6.37	6.50	6.45	7.71	7.81	7.47	6.99	6.68
Al iv	1.63	1.50	1.55	0.29	0.19	0.53	1.01	1.32
Al vi	0.50	0.62	0.63	0.20	0.09	0.16	0.20	0.51
Ti	0.07	0.07	0.08	0.01	0.00	0.02	0.02	0.07
Cr	0.00	0.00	0.00	0.00	0.00	0.00	0.00	0.01
Fe3+	0.58	0.63	0.59	0.06	0.00	0.25	0.51	0.42
Fe2+	1.26	1.10	1.15	1.81	1.80	1.74	1.77	1.26
Mn	0.04	0.03	0.03	0.05	0.21	0.13	0.14	0.03
Mg	2.54	2.54	2.53	2.87	2.89	2.70	2.35	2.71
Ca	1.83	1.79	1.78	1.92	2.01	1.92	1.92	1.83
Na	0.63	0.46	0.52	0.12	0.06	0.19	0.33	0.50
K	0.11	0.06	0.10	0.05	0.01	0.06	0.10	0.09
OH*	2.00	2.00	2.00	2.00	2.00	2.00	2.00	2.00
XMg	0.67	0.70	0.69	0.61	0.62	0.61	0.57	0.68
XFe3+	0.54	0.50	0.48	0.23	0.04	0.60	0.72	0.45

Table 2 cont.

Feldspar

Sample	AN1709D	AN1704A	AN1704A	AN1709A	AN1709A
Anal. #	3	67	68	1	2
SiO2	68.48	65.71	65.43	62.37	61.80
TiO2	0.03	0.06	0.01	0.01	0.00
Al2O3	20.61	18.91	18.89	22.67	23.04
Cr2O3	0.00	0.00	0.00	0.00	0.00
FeO	0.02	0.04	0.08	0.19	0.08
MnO	0.02	0.01	0.06	0.00	0.03
MgO	0.00	0.00	0.00	0.00	0.01
CaO	0.04	0.03	0.03	4.06	4.45
Na2O	12.51	0.12	0.16	9.86	9.63
K2O	0.04	15.94	16.10	0.10	0.10
Total	101.75	100.82	100.76	99.26	99.13
O#	8	8	8	8	8
Si	2.95	3.00	2.99	2.79	2.77
Al	1.05	1.02	1.02	1.19	1.22
Ti	0.00	0.00	0.00	0.00	0.00
Fe	0.00	0.00	0.00	0.01	0.00
Mn	0.00	0.00	0.00	0.00	0.00
Mg	0.00	0.00	0.00	0.00	0.00
Ca	0.00	0.00	0.00	0.19	0.21
Na	1.05	0.01	0.01	0.85	0.84
K	0.00	0.93	0.94	0.01	0.01
Or	0.18	98.71	98.36	0.53	0.54
Ab	99.65	1.13	1.49	81.03	79.24
An	0.16	0.17	0.16	18.44	20.22

Table 2 cont.

Clinopyroxene

Sample	AN1709a	AN1709a	AN1709a	AN1709a	AN1704A	AN1704A	AN1709E	AN1709E
Anal. #	1	2	3	4	1	2	1	2
SiO2	53.76	54.26	53.59	53.37	53.76	54.26	52.65	52.11
TiO2	0.03	0.08	0.01	0.10	0.03	0.08	0.03	0.02
Al2O3	1.32	1.45	1.42	1.93	1.32	1.45	0.54	0.65
Cr2O3	0.06	0.00	0.03	0.04	0.06	0.00	0.03	0.00
FeO	5.74	5.89	5.51	6.38	5.74	5.89	10.61	11.20
MnO	0.57	0.68	0.71	0.56	0.57	0.68	1.40	1.24
MgO	14.47	14.48	14.74	14.28	14.47	14.48	11.12	10.84
CaO	24.41	24.23	24.08	24.39	24.41	24.23	23.22	22.77
Na2O	0.57	0.60	0.49	0.65	0.57	0.60	0.58	0.91
K2O	0.01	0.01	0.04	0.03	0.01	0.01	0.04	0.01
Total	100.93	101.68	100.63	101.74	100.93	101.68	100.24	99.74
Formula Unit								
O#	6	6	6	6	6	6	6	6
Si	1.96	1.97	1.96	1.94	1.96	1.97	1.99	1.97
Ti	0.00	0.00	0.00	0.00	0.00	0.00	0.00	0.00
Al	0.06	0.06	0.06	0.08	0.06	0.06	0.02	0.03
Cr	0.00	0.00	0.00	0.00	0.00	0.00	0.00	0.00
Fe3+	0.05	0.04	0.05	0.09	0.05	0.04	0.05	0.09
Fe2+	0.12	0.14	0.12	0.11	0.12	0.14	0.29	0.26
Mn	0.02	0.02	0.02	0.02	0.02	0.02	0.04	0.04
Mg	0.79	0.78	0.80	0.77	0.79	0.78	0.63	0.61
Ca	0.96	0.94	0.94	0.95	0.96	0.94	0.94	0.92
Na	0.04	0.04	0.04	0.05	0.04	0.04	0.04	0.07
K	0.00	0.00	0.00	0.00	0.00	0.00	0.00	0.00
XMg	0.87	0.85	0.87	0.88	0.87	0.85	0.68	0.70
En	0.42	0.42	0.43	0.42	0.42	0.42	0.34	0.34
Fs	0.07	0.07	0.06	0.06	0.07	0.07	0.16	0.15
Wo	0.51	0.51	0.51	0.52	0.51	0.51	0.51	0.51

Table 3

Sample	Material	Steps (n)	Spectrum				
			% ³⁹ Ar	Age ± 1.96σ	MSWD (P)	TGA ± 1.96σ	K/Ca ± 1.96σ
AN1704A	Amphibole	13-16(4)	73.1	106.38 ± 2.18	1.21(0.31)	106.58 ± 2.17	0.07 ± 0.001
AN1709A	Amphibole	18-22(5)	46.33	106.06 ± 1.27	1.09(0.36)	108.61 ± 1.58	0.12 ± 0.001

Inverse Isochron			
Age $\pm 1.96\sigma$	MSWD (P)	Trapped $^{40}\text{Ar}/^{36}\text{Ar}$	Spread (%)
107.73 \pm 6.29	1.68(0.19)	293.01 \pm 24.53	33.9
104.75 \pm 1.96	0.54(0.65)	306.27 \pm 9.29	38

Table 4

AN1709a	H	Si	Al	Ca	Mg	Fe	Na	Ti	O	XFe3+
dry	0.00	53.26	15.67	9.93	12.11	8.63	8.16	1.03	0.500	
wet	14.82	49.30	14.51	9.19	11.22	7.99	7.55	0.95	0.477	
SS	7.41	51.28	15.09	9.56	11.66	8.31	7.85	0.99	0.49	0.12
LOI	8.89	51.68	15.20	9.63	11.75	8.37	7.91	0.99	0.49	
dry	0.00	53.09	15.62	9.89	12.08	8.60	8.13	1.02	0.818	
wet	14.78	49.16	14.46	9.16	11.18	7.97	7.53	0.95	0.76	
SS	7.39	51.13	15.04	9.53	11.63	8.28	7.83	0.99	0.79	0.19
LOI	8.87	51.52	15.16	9.60	11.72	8.35	7.89	0.99	0.79	
dry	0.00	52.95	15.58	9.87	12.04	8.58	8.11	1.02	1.07	
wet	14.74	49.05	14.43	9.14	11.16	7.95	7.51	0.95	0.995	
SS	6.93	50.88	14.97	9.48	11.57	8.24	7.79	0.98	1.03	0.25
LOI	8.85	51.39	15.12	9.58	11.69	8.33	7.87	0.99	1.04	

XH2O
0
1
0.5
0.6
0
1
0.5
0.6
0
1
0.47
0.6